High energy ion channeling - Principles and typical applications

C. Cohen, D. Dauvergne

High Energy Ion Channeling. Principles and typical applications.

C. Cohen * and D. Dauvergne **

* *GPS, Universités Paris VI-Paris VII, 2, place Jussieu, 75251 Paris cedex 05, France*
** *IPNL-CNRS/IN2P3, Université Lyon I, 4 rue E.Fermi, 69622 Villeurbanne cedex, France*

Abstract

The paper presents a review on selected aspects of high-energy ion channeling. Ion trajectories and fluxes are obtained in the frame of the "continuum model", in which atomic strings or planes are considered as uniformly charged objects. Computer simulations treating the consecutive binary collisions are also presented. Some typical applications are described, which take mostly benefit of the development of a highly non-uniform ion flux strongly peaked far from the heart of target atoms. These applications concern of course particle-matter interactions through, for instance, refined studies of the impact parameter dependence of energy loss and of charge exchange processes. They also concern material and surface science or nuclear physics, through lattice location measurements.

PACS: 61.85.+p; 34.70.+e
Keywords: Channeling, Blocking, Energy loss, Charge exchange.

I. Introduction

When a beam of swift ions enters a single crystal along a major crystallographic planar or axial direction, one observes a spectacular reduction of the yield associated to events that imply close nuclear encounters (nuclear reaction, large angle elastic scattering, formation of core-shell electron vacancies on target atoms and corresponding X-ray emission…). All these effects are characteristic of a phenomenon called Channeling, discovered and explained 40 years ago [1]. Channeling is the direct consequence of the fact that, in the particular beam-crystal geometry described above, the ions experience strongly correlated binary collisions with target atoms. These collisions focus the beam far from the atomic strings or planes of the crystal. Thus, the uniform flux associated to an ion beam impinging a crystal surface becomes progressively highly non-uniform as the ions penetrate in the bulk, with a pronounced maximum at the center of the "channels" delimited by the atomic rows or planes. We will briefly show in section II how one can very precisely calculate ion trajectories and fluxes in crystals. The knowledge of the ion's flux can be exploited in many ways, illustrated in section III. First one can determine the crystallographic location of a given population of nuclei inside a crystal by studying the associated yield of close nuclear encounter events. Such studies are beneficial in material science for the localization of impurity lattice sites, of defects, of surface atom relaxation, of strains in epitaxial layer growth…[2]. But they are also beneficial in nuclear physics when determining the pathlength before fragmentation of nuclei that have first been excited by violent collisions at regular crystal lattice sites, and thus the lifetime of these nuclei [3-5]. The second interesting feature of the non-uniform flux of channeled ions is that it permits to study specifically the interaction, at given impact parameter, of these ions with target electrons and particularly with loosely bound valence or conduction electrons. When the projectile is much faster than the electrons of the medium, one can use a crystal as a very dense quasi-free electron gas target and study charge exchange processes. Such studies, presented in section IV, concern electron impact ionization or excitation (EII or EIE) [6,7], radiative electron capture (REC) [8] (that is the reverse of the photoelectric effect), resonant transfer and excitation (RTE) [9] (the reverse of the Auger effect), or nuclear excitation by electron capture (NEEC, the reverse of internal conversion). One can also study in detail the impact parameter dependence of ion energy loss and determine the contribution of local and non-local interactions in this process [7,10,11,12]. Finally, we will show in section V that one can also exploit the fact that the correlated binary collisions of channeled ions with target atoms are quasi-periodic in time: this may induce resonant coherent excitation, populating excited atomic or nuclear levels [13-16].

II. Ion trajectories and fluxes in channeling geometry

1. Shadow behind an atom

Let us consider the situation represented in Fig. 1. A uniform flux of ions impinges on the first of a pair of atoms, the incident beam direction being parallel to the axis joining the two atoms. Each ion is repelled by the screened Coulomb potential generated by the first atom, the smaller the impact parameter the stronger the deflection. The result is the formation of a shadow cone of radius R at the level of the second atom. Roughly (and strictly in the case of a Coulomb potential), R is proportional to $(Z_1Z_2d/E)^{1/2}$, where Z_1 and Z_2 are respectively the atomic numbers of the ions and of the atom, d the distance between the pair of atoms and E the ion energy. A typical order of magnitude is R= 0.1 Å for E = 0.1 MeV/u and d = 3 Å, i.e. a typical interatomic distance. Thus, if the two atoms are on the fixed positions shown in Fig. 1, there will be no close nuclear encounter on the second one. Assume now that the relative positions of the two atoms, perpendicularly to the mean axis, may fluctuate with a standard variation ρ. It can then be demonstrated that the close encounter yield on the second atom is only a function of the ratio ρ/R. In the following we will choose to normalize these yields to the ones corresponding to a uniform ion flux.

Let us now consider an ion beam entering a crystal parallel to low index atomic rows with a uniform impact parameter distribution. One can use Monte Carlo simulations to calculate ion trajectories resulting from a sequence of binary collisions characterized by a realistic screened Coulomb potential. In such simulations, the instantaneous positions of the crystal atoms, with respect to their mean site, that are sampled by a given ion are determined through the thermal vibration laws. Once a set of trajectories is calculated, the ion fluxes and thus the close nuclear encounter yields can be readily obtained. We present in Fig. 2, from ref. [17], the result of a Monte-Carlo simulation providing the close nuclear encounter yield, as a function of penetration depth, for 10 MeV protons entering a tungsten crystal parallel to a <011> direction. After some marked oscillations, this yield becomes independent of penetration depth and levels around 2%. At the very surface, the yield corresponds to the uniform entrance flux and is thus equal to 1. We will show in section III how the very strong first peak yield can be used to provide information on the surface structure of crystals. As an example, we also show in Fig. 3 the calculated variation with the penetration depth of the ion flux at distances larger than r_{min} =1.2 Å from any atomic string when a beam of 10 MeV protons enters a silicon crystal along the <110> direction. The normalization is made with respect to a uniform ion flux. One can see in the figure a marked flux peaking effect far from atomic strings: after some oscillations this flux stabilizes at a value around 2. The latter value is of course determined by the chosen cut-off r_{min}.

2. Averaged continuum potentials, transverse energy conservation

Rather quantitative assessments can be made when introducing reasonable approximations in order to replace the numerical calculations presented above by an analytical description of the channeling phenomena. The discrete series of binary collisions with atoms can be approximated by a continuous interaction between a projectile and uniformly charged strings or planes. In this frame, simple physical quantities that govern the behavior of the projectile population in the crystal are introduced and general trends can be predicted with the help of statistical physics.

Calling V the screened Coulomb ion-atom potential and z the penetration depth, the axial continuum potential U(r) at the distance r from a string is:

$$U(r) = \frac{2}{d}\int_0^\infty V\left[\left(r^2 + z^2\right)^{1/2}\right]dz \qquad (1)$$

where d is the inter-atomic spacing.
The planar potential Y(y) at distance y from a plane is given by:

$$Y(y) = Nd_p\int_0^\infty \mathbf{2}\pi r V\left[\left(y^2 + r^2\right)^{1/2}\right]dr \qquad (2)$$

where d_p is the distance between two adjacent atomic planes.
In what follows we shall restrict ourselves to the description of axial channeling. We show in Fig. 4 from ref. [12] the axial potential map in a plane perpendicular to the (110) axis of a silicon crystal. This map has been obtained by summing the axial potentials, given by relation (1), corresponding to the six rows represented in the figure and by setting to zero the value of the potential at the channel center.

The motion of ions of kinetic energy E in the transverse plane is characterized by the conservation of the "transverse energy" $E_\perp$. The latter is determined by the entrance conditions and, in the small angle approximation, is given by:

$$E_\perp = QU(r) + E\Phi^2 = QU(r_i) + E\Phi_i^2, \qquad (3)$$

In relation (3), relativistic corrections are neglected. Φ is the angle between the ion's trajectory and the atomic string at position r, while Φ_i and r_i are respectively the entrance angle and impact parameter. In this paper, we are interested in swift ions, that are most of the time highly stripped and can thus be assimilated to point charges $Q = Z_1$-n, n being the number of core electrons, bound close to the ion's nuclei. Unless specified, we will use $Q=Z_1$ in the following. Relation (3) allows one to calculate the ion trajectories.

It is worthwhile to discuss the validity of the approximations that have been introduced in the present subsection. If one considers a set of binary collisions, $E_\perp$ changes abruptly at each collision, because the angle Φ changes at a fixed distance from the string. Then, between two collisions, this change is somewhat compensated because the potential component of $E_\perp$ changes continuously, as does the distance of the ion to the string, while the angle Φ is constant. A good check of the continuum approximation is to test up to what extent this compensation does conserve $E_\perp$. For this purpose, one may calculate the value of $E_\perp$ at the half-way plane between the $(i-1)^{th}$ and the i^{th} atom of a string, using the continuum potential. The continuum approximation holds if the binary collision with the i^{th} atom does not induce a significant change of $E_\perp$ calculated at the half-way plane between the i^{th} and the $(i+1)^{th}$ atom of the string. The result is that $E_\perp$ is conserved at the first order and thus the continuum model represents a good approximation as far as the minimum distance of approach to a string remains larger than $r_{lim} = (b_o.d)^{1/2}/2$. Here, b_o is the collision diameter associated to the Coulomb potential, which is inversely proportional to the square of the ion velocity. Thus, as could be expected, the smaller the interatomic distance and the larger the ion velocity, the more accurate the continuum model.

Of course, the instantaneous positions of the crystal atoms in the transverse plane scatter around their mean values along the strings. The corresponding distribution is characterized by the two-dimensional rms. thermal vibration amplitude ρ. This weakens the correlation between successive binary collisions and induces incoherent multiple scattering

which, in the average, increases $E_\perp$. Such a process, called dechanneling, becomes very important when the ions can approach the strings at distances of the order of ρ, i.e. when their transverse energy is large. However, even ions with a low initial $E_\perp$ experience incoherent multiple scattering by collisions on target electrons. Thus, their transverse energy also increases on the average, but much more slowly.

It is convenient (but somewhat arbitrary) to set a limit to the transverse energy, $E_{\perp lim}$, above which an ion cannot be considered as channeled. One can decide, for instance, that this is the case for ions that can approach strings at distances smaller than ρ and thus experience close nuclear encounter events. With this definition, one has: $E_{\perp lim} = Z_1 U(\rho)$. It can be seen in Fig. 4 that when a uniform ion flux impinges on a crystal surface, most of the ions get a potential energy much smaller than $U(\rho)$. Then, roughly, they will reach a transverse energy above $E_{\perp lim}$ if the beam entrance direction makes an angle Φ_i with the string greater than a critical value Ψ_C given by:

$$E\Psi_C^2 = Z_1 U(\rho) \qquad (4)$$

Ψ_C is called the channeling critical angle. Its value depends of course on the choice of the screened interatomic potential. A good estimate has been provided by Lindhard [1] for axial channeling:

$$\Psi_C = (2Z_1 Z_2 e^2/Ed)^{1/2} \qquad (5)$$

3. Ion flux at statistical equilibrium

The knowledge of the particle trajectories provides the determination of the ion flux $P(\vec{r}, z)$ at any point of the crystal. In fact, as already indicated in subsection 1, one can clearly see in Fig. 2 that after some penetration depth the close nuclear encounter yield, and thus the ion flux near strings, becomes independent of depth. This is also true far away from the strings, as seen on Fig. 3, and, more generally, at any point of the transverse plane. This feature reflects the establishment of a statistical equilibrium where all the available configurations in the transverse phase space of an ion of given $E_\perp$ are equiprobable. The incoherent multiple scattering events described in subsection 2 accelerate significantly the establishment of equilibrium. The latter is reached while the $E_\perp$ distribution is still only marginally affected by multiple scattering. Let us call $P_\infty(r \mid E_\perp)$ the contribution of ions of transverse energy $E_\perp$ to the flux at statistical equilibrium, at distance r from an atomic string. It can be shown that:

$$P_\infty(r \mid E_\perp) = \begin{cases} 2\pi r/A(E_\perp) & \text{for} \quad U(r) < U(r_{E\perp}) \\ 0 & \text{for} \quad U(r) > U(r_{E\perp}) \end{cases} \qquad (6)$$

Expression (6) is fully valid only close enough to atomic strings, i.e. in regions where equipotential lines are circular. $A(E_\perp)$ is the available area of the transverse space for the ion considered and $r_{E\perp}$ its minimum distance of approach to the strings. One can associate to each string a unit cell in the transverse plane, centered on the string and with a radius r_0 given by:

$$\pi r_0^2 = 1/Nd \qquad (7)$$

The overall flux $P_\infty(r)$ at statistical equilibrium is then obtained by integrating over all

transverse energies, each $E_\perp$ being affected with a weight given by the transverse energy distribution $g(E_\perp)$:

$$P_\infty(r) = \int_0^\infty g(E_\perp) P_\infty(r|E_\perp) dE_\perp \qquad (8)$$

For a beam entering parallel to a string, the integration of relation (8) leads to the very simple result:

$$P_\infty(r, \Phi_i = 0) = (2r/r_0^2) \ln (r_0^2/(r_0^2 - r^2)) \qquad (9)$$

4. Blocking; rule of reversibility

Let us first consider a beam of ions (Z_1, E) entering a crystal with a uniform distribution of entrance impact parameters, and with an entrance angle distribution characterized by a mean value Φ, with respect to a given crystallographic direction, and by a spread of rms. $\Delta\Phi$. The corresponding flux distribution at a point $(\vec{r}, z)$ in the crystal is noted $P_{in}(\vec{r}, z, \Phi, \Delta\Phi)$. Let us now consider an isotropic emission of the very same ions (Z_1, E) from the very same point of the crystal, $(\vec{r}, z)$, and call $P_{out}(\vec{r}, z, \Phi, \Delta\Phi)$ the flux of ions emerging from the crystal observed by a detector placed at an angle Φ, with an aperture corresponding to an angular spread of rms. $\Delta\Phi$. It can be demonstrated, using the Liouville theorem, that:

$$P_{in}(\vec{r}, z, \Phi, \Delta\Phi) = P_{out}(\vec{r}, z, \Phi, \Delta\Phi) \qquad (10)$$

Let us call $\chi_{in}(\Phi)$, or channeling yield, the close nuclear encounter yield on any population of atoms of given spatial distribution inside the crystal for a beam entering with the angle Φ. The consequence of relation (10) is that, whatever Φ, $\chi_{in}(\Phi)$ is equal to the yield $\chi_{out}(\Phi)$ of ions leaving the crystal along Φ after being emitted by the very same atom population. $\chi_{out}(\Phi)$ is called the blocking yield. The equality between channeling and blocking yields is well verified experimentally [18]. The blocking effect is schematized in Fig. 1: the scattering by an atom generates a "blocking cone" in the initially isotropic angular distribution. The blocking cone axis is along the axis of the atomic pair.

We show in Fig. 5 a typical blocking pattern registered on a position sensitive detector [5]. A 24 MeV/u ^{238}U beam was transmitted through a 6 μm thick Si crystal. The incident angle was set a few degrees off the <110> crystal axis and the detector was placed in order to intercept the ions that were elastically scattered in the vicinity of the <110> direction. The darker the pattern, the larger the number of ions intercepted. The central bright spot of the pattern corresponds to the intersection of the <110> direction by the detector plane, and, obviously, the emission yield in this direction is very weak. One also observes weak emission along the lines that correspond to the intersection of crystallographic planes with the detector plane. The inset represents the one-dimensional blocking pattern integrated over the azimuth angles and centered along the axial direction. The emission yield $\chi(\Phi = 0)$ is very small, around 3%.

We will show in section III that the blocking effect is used to bring valuable and specific information in surface physics, concerning surface lattice sites. We will also show that it is a very powerful tool for the determination of the lifetime of excited nuclei before

fragmentation.

Recently, a departure from the reversibility rule has been observed when heavy ions, around 1 MeV/u with an initially isotropic distribution are transmitted through thin crystals [19]. This effect that can, at least partially, be attributed to charge exchange processes will be discussed in section IV.

5. Validity of a classical description for high energy ion channeling

The criterion of validity for a classical description of a binary collision between particles depends on the interaction potential. The problem has been analyzed in detail by Bohr [20]. For a Coulomb potential, a classical description holds if the wavelength $\lambda\!\!\!^{-}$ associated to a particle with a velocity equal to the relative velocity v between collision partners and with a mass equal to the reduced mass, $\mu = M_1M_2/(M_1+M_2)$, is small at the scale of the collision diameter: $b_0 = 2Z_1Z_2e^2/\mu v^2$. Calling $v_0 = e^2/\hbar$ the Bohr velocity, this implies that the so-called "Bohr parameter" κ must obey the following relation:

$$\kappa = b_0 / \lambda\!\!\!^{-} = 2Z_1Z_2 v_0 / v > 1 \ . \qquad (11)$$

In channeling, one deals with the ion motion in the transverse plane. In the frame of the continuum approximation, one must then ask whether the collision of an ion with maximum transverse velocity $v_{\perp C} = v\Psi_C$ with a continuous string can be treated classically. The first observation is that, as the critical Ψ_C is inversely proportional to v, the condition searched should be independent of the longitudinal ion velocity. This is indeed the case. With some realistic approximations concerning the axial potential given by relation (1), it can be shown that the transverse motion of a charged particle of mass M_1 can be described classically as long as

$$(M_1/m_e)^{1/2} >> 1 \qquad (12)$$

m_e being the electron mass. This relation is thus obviously fulfilled for ions. Thus, in the frame of the continuum model, ion channeling can always be treated classically, which is not the case for electron channeling.

It is also important to check up to what extent the spreading of the ion-wave packet induced by successive collisions could affect the validity of the continuum model. This is a tough question. Let us call *a* the screening radius associated to the screened interatomic potential V . It can be shown that, as long as the critical angle remains smaller than about *a*/d (a value around 10^{-1} rad), the wave-packet associated to the ion retains its width during its collision with a string. This is the case for swift ions above typically 100 keV/u. In such a situation, it can also be shown that $E_\perp$ fluctuations can be neglected. The continuum approximation and the $E_\perp$ conservation are thus not affected by quantum fluctuations for high-energy ions.

III. Determination of lattice sites: applications to Material Science and Nuclear Physics

1. Material science

1.1 Lattice location of impurities

Consider an ion beam entering a crystal with an incident direction characterized by an angle Φ. We have shown in section II how the non-uniform ion flux in channels, and, consequently, the yield $\chi(\Phi)$ of close nuclear encounter with any population of atoms inside a crystal could be calculated. Conversely, it is possible to determine the lattice sites occupied by a population of atoms inside a crystal by studying the corresponding close nuclear encounter yields $\chi(\Phi)$. Practically, one attempts to fit the values $\chi(\Phi)$ measured experimentally in the vicinity of various crystallographic directions, with yields calculated assuming various distributions of occupied sites. This is illustrated in Fig. 6, from ref. [21]. The aim of the experiment was to determine the location of deuterium atoms implanted in a bcc tungsten crystal. The implanted deuterium was characterized via the $D(^3He,p)^4He$ nuclear reaction. The angular dependence of the yield associated to this reaction, in the vicinity of the <100> direction, clearly shows that the implanted atoms occupy tetrahedral sites.

1.2 Heteroepitaxy

Another interesting example is the determination of lattice strains when thin layers of a species A are epitaxially grown on the top of a crystalline substrate of a species B. The strains result from the lattice mismatch between the meshes of A and B. If the mismatch is not too strong, and if the layer A is not too thick, atoms A will be located in registry with atoms B. If, for instance, the lattice parameter of A, a_A, is larger than a_B, layer A will then be compressed in the plane parallel to the substrate surface and, in compensation, it will experience a tensile strain perpendicularly to this plane. The corresponding tetragonal distortion can be determined in channeling experiments. Assume cubic meshes and a (001) surface orientation. The result of the tetragonal distortion is that the <011> axes of A and B are not exactly parallel. The corresponding angular shift can be evidenced when comparing channeling dips, $\chi(\Phi)$, in the vicinity of the <011> direction corresponding to close nuclear encounter on A and B atoms respectively. A typical example, from ref. [22], is shown in Fig. 7. It corresponds to the growth of an Fe layer (of bcc structure) on the top of a (001) GaAs substrate (of diamond structure). One has $2a_{Fe}/a_{GaAs} = 1.015$. As a consequence, the Fe layer is compressed in the (001) plane. This is well evidenced when comparing the position of the minima corresponding to the channeling angular scans associated respectively to Fe and to GaAs, in the vicinity of the <011> direction. When the sample is heated above 450°C, Fe reacts with GaAs and forms a three-atomic compound, FeGaAs, in the interface region. The position of the minimum of the channeling angular scan, across <011>, associated to the non-reacted part of the deposit in the surface region (pure Fe) is also compared in Fig. 7 to that of the substrate. This comparison clearly shows that the presence of the reacted layer at the interface reverses the strain experienced in the (001) plane by the Fe film, from compressive to tensile.

1.3 Surface studies

Channeling experiments also provide very interesting information on the structure of the very surface of crystals. As an example, Fig. 8, from ref. [2], shows the comparison between two energy spectra of backscattered ions, obtained with a 2 MeV ^{4}He beam incident on a W crystal. The first one corresponds to a "random" orientation of the beam far from any major crystallographic direction. For the second spectrum, the beam was aligned along a <100> axis. The energy scale in the abscissa can be related to a depth scale, *via* the energy loss of ions in the crystal: the highest energy corresponds to backscattering events at the crystal surface. It clearly appears in Fig. 8 that the backscattering yield in the bulk of the crystal is reduced by about two orders of magnitude in the axial channeling geometry. However, there is a marked peak yield in the corresponding spectrum, associated to backscattering events in the very near surface region. This "surface peak" is related to the strong and narrow peak yield predicted, in the same region, by the Monte-Carlo simulations shown in Fig. 2. Its integral is related to the penetration depth required for the development of the shadow cone, and is usually expressed in "number of atoms per row". Let us call α_i the normalized backscattering yield on the i^{th} atom of a row. As the entering ion flux is uniform, one has $\alpha_1=1$. As seen in Fig. 2, α_i decreases rapidly with i in the very near surface region, and thus, the sum $S = \Sigma_i\alpha_i$ converges rapidly. This sum is the integral of the surface peak expressed in number of atoms per row. Monte-Carlo simulations demonstrate that, for a perfect crystal, S is a unique function of the ratio ρ/R, ρ being the two-dimensional rms. amplitude of the atom thermal vibrations perpendicularly to the strings, and R the radius of the shadow cone, as illustrated in Fig. 1. The relation between S and ρ/R is represented in Fig. 9, from ref. [23], which shows the result of many simulations performed on various ion-crystal couples. Practically, for ions between 0.1 and 1 MeV/u, the ratio ρ/R is of the order of 1, and S is thus of the order of 2 (see Fig. 9). Consequently, its value is mainly related to the shadowing efficiency of surface atoms on subsurface atoms. It then provides direct information on the lattice location of surface atoms. We now give some illustrations of surface studies.

Fig. 10, from ref. [24], represents the evolution of S as a function of temperature T, in a Pb crystal with a (101) surface. As ρ varies roughly like $T^{1/2}$, S is expected to increase with T. The full line I represents the simulated variation of S assuming that surface atoms vibrate like bulk atoms. The full line II is the result of simulations in which the vibrations of surface atoms are larger (by about 50%) than those of bulk atoms. Up to 450 K, this line fits very well the experimental results, represented by the points in the figure. Thus these measurements provide a precise determination of the surface thermal vibration amplitude. But the most striking observation is the strong and increasing discrepancy between the simulated and measured values of S above 450 K, i.e. well below the temperature of the first order phase transition leading to bulk melting (600 K). The effect is reversible in T. The very high values of S measured above 450 K demonstrate the establishment of a strong surface disordering, thermally activated. The authors have been able to study the depth over which such a disorder extends, as a function of temperature, and have assigned these results to surface pre-melting.

Information can also be reached on the very first steps of epitaxy, as illustrated in Fig. 11 from ref. [2]. The authors have deposited increasing quantities of Au, from 0 to 4 monolayers on top of an Ag crystal (Ag and Au have the same mesh and the same lattice parameter). The figure represents backscattering spectra registered in axial alignment geometry at various steps of the deposit. One clearly sees the gold peak appearing in the high-energy part of the spectra, the integral of which saturates when the deposited quantity exceeds 3 monolayers. In the mean time, the Ag surface peak weakens continuously and disappears when the Au deposit exceeds 3 monolayers. This behavior demonstrates: i) that the deposition proceeds *via* a layer by layer growth mode (no Au islanding). ii) That the deposited Au forms

a good single crystal. iii) That the Au crystal is in perfect epitaxy with the Ag substrate, which leads to the shadowing of the Ag atoms by Au atoms and thus to the disappearance of the Ag surface peak.

We now present an illustration related to surface relaxation. One consequence of the discontinuity corresponding to the surface is that the lattice sites of the surface atoms differ from those of bulk atoms. For symmetry reasons this corresponds to a coherent displacement, i.e. to an expansion or a contraction of the first interplanar distances. These relaxations can be measured by channeling in the very same way than the tetragonal distortions described above in the case of the Fe/GaAs system. However, in the present case, this distortion concerns the surface atoms of the substrate instead of deposits. One can then perform angular scans across an axis not perpendicular to the crystal surface and compare the angular position of the minima corresponding respectively to the bulk yield (unstrained region) and to the surface peak yield (strained region). This provides a measurement of the surface relaxation. We show in Fig. 12 from ref. [25] an even more sophisticated illustration of this type of studies, performed on a Cu crystal, the surface orientation of which, (4,1,0), makes a small angle with respect to the (100) plane. Such a surface (called "vicinal") self-organizes in (100) terraces of equal length separated by periodic steps of <001> orientation. As surface atoms relax with respect to regular bulk lattice sites, one expects that step edge atoms should relax with respect to other surface atom lattice sites. This is clearly evidenced in the angular blocking scans shown in Fig. 12. These scans were performed across the <011> axis contained in the plane of the terrace, by moving a tightly collimated detector perpendicularly to this plane. Of course, the minimum of the bulk yield corresponds to a detection angle of 90°, i.e. when the detector is along the axis. But the angular positions of the blocking scans corresponding to the surface peak are different, as seen on the figure. Roughly, these positions are related to the direction along which the edge atoms shadow the other surface atoms. They provide thus the edge atom relaxation. One sees on Fig. 12 that for a bare Cu surface this relaxation is a contraction towards the crystal bulk below the surface plane, while, when the Cu surface is covered by one monolayer of oxygen, the relaxation becomes an expansion above the surface plane.

1.4 Characterization of defects

We have just seen that detailed information can be brought on the sites occupied by surface or step edge atoms by studying the behavior of the surface peak, for instance by means of backscattering spectra. One can also use backscattering experiments in channeling geometry to determine the displacements from regular lattice sites of bulk atoms, i.e. to study lattice defects. This is well illustrated in Fig. 13, from ref. [26]. A nickel single crystal was implanted, in its near surface region, by Sb ions (the implantation energy was 80 keV, corresponding to a range of 250 Å). Fig. 13 shows various backscattering spectra, corresponding to different implantation fluences, in which the probing beam (2 MeV ^{4}He ions) was aligned with a <110> crystallographic direction. It also shows two random backscattering spectra, corresponding respectively to a low and a high implantation dose. In Fig. 13, the higher the channel number the greater the energy of the backscattered ions. The high-energy peak corresponds to backscattering on Sb atoms, and the lower energy plateau to backscattering on Ni atoms. On this plateau, the lower the energy, the deeper the depth at which a backscattering event took place. In the random spectrum corresponding to a high implantation fluence, one observes a lowering of the high-energy part of the Ni plateau, corresponding to backscattering events on Ni atoms in the shallow region were Sb was implanted. This is related to the change of composition in this region. But the most interesting observation is the very strong influence of implantation on the aligned spectra. When the implantation fluence increases, one can notice the development and broadening of a peak of

scattering yield on Ni atoms in the implantation zone. In the same time, there is a strong increase of the backscattering yield corresponding to the deeper part of the sample. One also observes a region just after the peak, in which the slope of the Ni plateau is stronger than at greater depths. All these behaviors are related to the implantation-induced displacement of Ni atoms from regular sites, along the path of the implanted species. These displacements have two main consequences on the interaction of the aligned ^{4}He probing beam with the crystal. First, the displaced Ni atoms are no more located in regions of the transverse plane where the ^{4}He ion flux is low. Thus, the backscattering yield on Ni increases in the near surface region corresponding to the implanted ion path; this is the origin of the backscattering yield peak observed. But one must also consider that there is an angular spread of the incoming ^{4}He beam when crossing this perturbed crystal region. As a consequence the transverse energy distribution associated to the beam is shifted towards larger $E_\perp$ values, which in turn increases the backscattering yield on Ni atoms even if they occupy regular lattice sites. This explains the increase of this yield, when compared to the one corresponding to an unimplanted crystal, even in deep regions where no defects are present. This "dechanneling effect" can be clearly seen in the region of the Ni plateau with high slope, behind the backscattering yield peak. In the corresponding depth interval, the fast increase of the backscattering level is more due to dechanneling than to direct encounter with displaced Ni atoms. In order to extract properly the depth distribution of the concentration of displaced atoms, one must then subtract properly the contribution of dechanneling, for instance behind the backscattering yield peaks of Fig. 13. Of course one must take into account the fact that this contribution steadily increases during the penetration of the probing beam in the perturbed region. The evaluation of the dechanneling rate is not easy as it depends strongly on the nature of the defects. For instance, the dechanneling induced by point defects is due to incoherent multiple scattering and one can show that dechanneling is in this case a decreasing function of the probing ion velocity. On the contrary, extended defects like dislocations induce a somewhat coherent beam bending, and, in this case, the dechanneling efficiency increases with the probing ion velocity. Finally, in order to check precisely the positions occupied by the displaced atoms, one must determine the close encounter yields along various crystalline directions, and, ideally, fit these yields through numerical simulations. The study of defects by ion channeling can then provide precise and quantitative information, but it is a difficult task.

2. Nuclear Physics: fission time measurements

These measurements are based on the fact that channeling and blocking yields $\chi(\Phi)$ corresponding to a given population of scattering or emitting centers crucially depend on the sites occupied by this population, with respect to regular lattice sites. To illustrate this feature, we show in Fig. 14, from ref. [27], three channeling dips, performed with the same incoming beam, across the <111> axis of a W crystal. The first one corresponds to backscattering events, the second to tungsten L-X-ray production, and the third to the emission of M-X-rays. The first two dips are nearly identical. Both of them imply collisions with W atoms at impact parameters much smaller than ρ, the 2-D rms. vibration amplitude of W atoms (the L-shell of W is well localized at this scale). On the contrary, for the M-shell, vacancies can already be produced at impact parameters somewhat larger than ρ. They may then originate from ions of transverse energy smaller than $Z_1U(\rho)$. The consequence is that the associated dip is narrower and that the minimum yield is significantly larger than in the first two cases. Of course, due to the reversibility principle, the same conclusions hold for blocking: the lower the potential energy associated to the position of the emitting centers, the narrower and the less pronounced

the dips. The analysis of such dips and, if necessary, their fit by simulations, should then provide the positions of the emitting centers.

This is the basis of the fission time measurements. Excited nuclei, decaying mostly by fission, are produced in a crystal by collision of energetic ions with crystal atoms (the incident ion beam is sent along a random direction in order not to extinct the collision probability). These excited nuclei recoil along a given direction with a velocity that can be determined by the kinematics of the collision. After a certain path, related to their lifetime and velocity, fission may occur, and the charged fragments will be emitted isotropically in the frame of the excited nuclei. These fragments will be submitted to the blocking effect to an extent that depends on the location, with respect to lattice sites, from which they are emitted (see the first paragraph of the present subsection). The analysis of the blocking dips appearing on position-sensitive fragment detectors should then provide the distribution of the time elapsed between the collision and the fission events. The shape of the dips and the associated minimum yields vary continuously when the emission point of the fragments is located at distances from atomic strings between 0.1 Å (typical order of magnitude of ρ) to a few Å (typical interatomic distances). The range of times that can then be reached will depend on the recoil direction and velocity. Practically the accessible time window is between a few 10^{-19} and 10^{-16}s.

The fissile excited nuclei that we are considering are complex dynamical systems. The time dependence of the fission probability depends on the interplay between cooling down (*via* evaporation of neutrons or of light charged particles and γ emission) and deformation towards the saddle point at which the fission process becomes irreversible. The velocity of the deformation is limited by the nuclear viscosity, which in turn depends on the time-decreasing nucleus temperature. Fission time measurements are thus expected to provide information on nuclear dissipation. The shape and extension of fission time distributions also depend strongly on the evolution with the residual excitation energy of the activation energies associated respectively to particle evaporation and to fission. The values reached by these activation energies at low residual excitation energy will determine the probability of fission events with long associated times. Such events are expected to occur for highly fissile nuclei.

One can then expect that the distribution of fission time should have complex shapes departing from a simple exponential decay characterized by a single decrement. In such a situation, the characterization of the distributions by only a mean "lifetime" is obviously insufficient. The existence of a very low tail extending towards very long times will drastically affect the mean lifetime without changing significantly the shape of the body of the distribution.

An interesting feature of lifetime measurements *via* the study of blocking yields is that the latter depend very much on the shape of the lifetime distribution and not only on mean values. This is clearly demonstrated on Fig. 15 from ref. [28] which represents the simulation of blocking dips in the vicinity of the <110> axis of a thin Si crystal for Z = 41 fission fragments generated by a 29 MeV/u Pb beam incident on the crystal 5° off the axis direction. In the simulations various mean lifetimes τ and various distribution shapes were assumed. For exponential shapes the blocking effect is maximum for $\tau \leq 3.10^{-19}$s. The blocking dip is already significantly narrower for $\tau = 10^{-18}$s, the blocking effect is highly reduced for $\tau = 10^{-17}$s, and disappears above $\tau = 10^{-16}$s. But the most striking effect displayed on Fig. 15 is the very strong difference between the blocking dip associated to an exponential decay characterized by $\tau = 10^{-17}$s, and the one associated to a two-component distribution of the same mean lifetime. The latter is the weighted sum of two exponential decays, the first one (97%) with $\tau_1 = 10^{-19}$s, and the second one (3%) with $\tau_2 = 3.10^{-16}$s. The weighted sum of τ_1 and τ_2 provides a value $\langle\tau\rangle = 10^{-17}$s. The lifetime associated to this distribution is thus fully dominated by the small component with long lifetime, but, of course, the blocking dip is mainly determined by the strong component with the short lifetime. It is thus much closer to

the dip with an exponential decay characterized by a decrement of 10^{-19}s than to the one with a decrement of 10^{-17}s. However, the influence on the dip of the weak component with a low lifetime is detectable if the experimental statistics is appropriate.

In fact, one of the major findings of blocking measurements is the unambiguous evidence that very long lifetime components ($\tau > 10^{-17}$s) frequently exist in the fission time distributions [4,5,28,29]. This is in no way an artifact related to the technique, as there are systems for which blocking experiments clearly show that there is no long lifetime [30]. Other techniques devoted to the measurement of fission times, such as the study of pre-scission emission multiplicity [31] are unable to reveal such components. However, in order to determine up to what extent the filling of the blocking dips is related to the existence of a long lifetime component, one must also search for all other possible contributions to this filling. This can be done in principle by registering blocking dips for ions produced in the very same crystal without any long lifetime component. This is the case of ions elastically scattered, giving rise to the blocking dip shown in Fig. 5. For such ions some filling of the dips may arise from the existence of crystal defects, but it can also be partially due to incoherent multiple scattering that may re-orient the trajectory of an ion parallel to crystallographic directions. This effect, called "feeding-in" is the reverse of the dechanneling effect mentioned in section II. There is still another source of feeding-in that is specific of fission fragments and thus does not affect the blocking dips of elastically scattered ions. This source is the post-fragmentation neutron emission. The efficiency of such an emission is maximal if it takes place when the fragment is far from strings or planes, i.e. if mostly all its transverse energy is kinetic. In such a situation the trajectory re-orientation induced by neutron emission may, for given emission directions, reduce the transverse energy of the fragment. The influence of post-fragmentation neutron emission is thus not only related to the mean number of emitted neutrons and to their energy distribution, but also to the time distribution of the emission. All these features can be predicted theoretically in a quite reliable way, and thus the effect of post-fragmentation neutron emission can be rather well accounted for.

Moreover, collisions between energetic ions and crystal atoms produce a wide variety of excited nuclei, with a wide range of excitation energies. These nuclei may fragment in a more or less symmetrical way. In order to extract interpretable data, one has to determine the lifetime distribution associated to a given type of fragmentation, from a given excited nucleus, with a given initial excitation energy. This has been achieved for instance in ref. [5], devoted to the study of the fission of uranium-like nuclei. Those were produced by collision of ions from a ^{238}U beam of 24 MeV/u with the nuclei of a Si crystal. The two fragments, A and B, produced after a collision were detected in coincidence, and their atomic numbers determined, using position-sensitive telescopes. For neutron rich nuclei like uranium, the charged particle evaporation is negligible and thus $Z_A + Z_B$ is the atomic number of the excited nucleus before fragmentation. Only events such that $Z_A + Z_B = 92 \pm 5$ were selected, and they thus arise from uranium-like excited nuclei. The initial excitation energy was determined by measuring, event by event, the neutron multiplicity, using a high efficiency 4π neutron detector inside which the goniometer supporting the Si crystal was placed. We show on Fig. 16, from ref. [5], the blocking dips associated to various ranges of neutron multiplicity, i.e. to various ranges of initial excitation energies. It clearly appears that the dips corresponding to low multiplicities, i.e. to low initial excitation energies, are the most filled. However, the width of the dips appears to remain rather constant, whatever the filling is. This behavior can only be interpreted by assuming that there is a two-component lifetime distribution with, respectively, a very short ($< 3.10^{-19}$ s) and a very long ($> 3.10^{-17}$ s) associated mean value. For high neutron multiplicities, i.e. strong initial excitation energies, the weight of the component with long mean lifetime is negligible. This weight continuously increases when the initial excitation

energy decreases, and may reach 30 to 40% for neutron multiplicities smaller than 4, which correspond to initial excitation energies smaller than 50 MeV.

To conclude, fission time measurements by the blocking technique bring specific information on long lifetime components. They also allow an analysis of the shapes of the time distributions.

IV Energy loss and charge exchange in channeling geometry: interaction with a dense, non-uniform electron gas.

We will first present general considerations on energy loss and charge exchange processes in subsections 1 and 2, respectively. The experimental results that are presented in subsections 3 and 4 often correspond to the "high velocity regime" in which the ions velocity is significantly larger than the mean orbital velocity of target or projectile electrons. In such a situation the ions are nearly fully stripped and can be considered as point charges. This is however not the case for the results presented in subsections 3.4 and 4; here the ions are in the" intermediate velocity regime", heavy ions may carry many electrons, not always highly localized in the nucleus vicinity, and charge changing cross sections are high.

1 Energy loss

1-a General considerations and theoretical approaches.

The slowing down of ions in crystals is strongly affected by channeling effects. The energy loss distribution $g(\Delta E)$ of an initially monokinetic ion beam transmitted through a crystal in channeling geometry is much broader than after transmission along a random direction. The mean energy loss is generally significantly smaller in channeling; the lower edge of $g(\Delta E)$ corresponds to losses that can be less than one half of the mean random loss, and the upper edge to losses that can be nearly twice the mean random loss. This is illustrated in Fig. 17 that shows the energy distributions of a Pb ion beam, with an initial energy of 29 MeV/u, after crossing a thin Si crystal, respectively along a random and a <110> axial orientation. In this figure, the energy losses in channeling geometry are normalized to the mean random loss, after taking into account a correction factor related to the different charge states at the crystal exit (see subsection IV-3-2). The very broad distribution observed in the axial case is related to the fact that ions with different $E_\perp$ explore different accessible transverse areas $A(E_\perp)$. Thus they sample different impact parameter distributions and electronic densities. The analysis of $g(\Delta E)$ can then provide information on the stopping power $S(E,r)$ at various distances r from the crystal axes or planes.

In order to interpret such data, an impact parameter description of the energy loss processes is required. In what follows, we will consider separately the contribution of rather localized and tightly bound core-shell target electrons and of the delocalized valence or conduction target electron gas. We will also suppose that ions can be described as point charges of fixed value Qe. Effects related to deviations from this behavior will be mentioned at the end of this subsection.

In what concerns the interaction with core target electrons, various impact parameter treatments, at different levels of approximation, are available. However, most of these treatments have restricted domains of applicability. These restrictions are related to the value taken by the Bohr parameter $\kappa = 2Qv_o/v$ characterizing the interaction of an ion of velocity v with an electron at rest.

If one has: *i)* $\kappa > 1$ and *ii)* $v > v_e$, where v_e is the orbital velocity of the target electron considered, a classical description of the slowing-down process can be used. In the corresponding theory, proposed by Bohr [20], target electrons are considered as classical oscillators. In random media the stopping power is then given by:

$$\frac{dE}{dx} = \frac{4\pi Q^2 e^4}{m_e v^2} NZ_2 \ln \frac{b_{max}}{b_{min}} = \frac{4\pi Q^2 e^4}{m_e v^2} NZ_2 \ln \frac{1.123\, m_e v^3}{Qe^2 \langle \omega \rangle} \qquad (11)$$

where N is the atomic density, $b_{max} = 1.123v/\langle\omega\rangle$ is a mean adiabatic cut-off (for $b > b_{max}$ the collision time exceeds the mean orbital period) and $b_{min} = b_o/2 = Qe^2/m_e v^2$. The mean frequency $\langle\omega\rangle$, is defined by $Z_2 \ln(\langle\omega\rangle) = \Sigma_f f_f \ln(\omega_f)$, where f_f are the dipole oscillator strengths and ω_f the frequencies associated to transitions between the atom ground state and well defined final states indexed by $_f$.

If $\kappa < 1$, i.e. at high ion velocities and/or low Q values, a perturbation quantum treatment is well adapted. In random media, it leads to the well-known Bethe stopping power [32]:

$$\frac{dE}{dx} = \frac{4\pi Q^2 e^4}{m_e v^2} NZ_2 \left[\ln \frac{2 m_e v^2}{\hbar \langle \omega \rangle} + \ln \gamma^2 - \beta^2 \right] \qquad (12)$$

where $\beta = v/c$, $\gamma = \left(1 - \beta^2\right)^{-1/2}$. $\hbar\langle\omega\rangle = I$ is the mean logarithmic excitation energy per electron associated to the mean frequency $\langle\omega\rangle$ already defined. Surveys of stopping power for fast ions can be found in refs. [33,34] and references therein. For practical use, the energy loss, the straggling (in energy and angular), the range of ions in matter, as well as effects related to collision cascades over a wide range of energy can be computed in "random media" by simulation codes like SRIM [35].

Recently, Schiwietz and Grande [36] have used the non-perturbative Bloch theory [37] to propose an approximate and simple impact parameter description that is valid in the whole range of impact parameters with respect to electrons, and that applies for any κ value. The Bloch stopping formula tends asymptotically towards the Bohr formula (11) and the Bethe formula (12) for respectively great and small κ values. In a first step, Schiwietz and Grande calculate the energy transfer $T(b_e)$ to a bound electron at impact parameter b_e. They find:

$$T(b_e) = T_{sudden}(b_e) \times h(v, \kappa, b_e) \times \sum_f f_f g\left(\frac{b_e \omega_f}{v} \right), \qquad (13)$$

where $T_{sudden} = 2Q^2e^4/m_e v^2 b_e^2$ is the energy transfer to a free electron when neglecting the electron recoil (momentum approximation). The summation, weighted by the dipole-oscillator strengths f_f, is performed over all the final states reached by transitions, with frequencies ω_f, that imply the considered electron. The functions h and g are explicitly given in ref. [36]. The function h tends towards 1 when b_e becomes larger than the shell radius b_{shell} of the bound target electron. For $b_e < b_{shell}$, the function h decreases rapidly, compensating the divergence of T_{sudden} when $b_e \to 0$. This divergence, without physical meaning, is related to the fact that the momentum approximation does not hold for collisions with small b_e at the scale of b_0 or of the wavelength associated to an electron of velocity v. The function g, the expression of which is already derived in ref. [38], depends only on the ratio between b_e and the adiabatic impact parameter cut off v/ω_f. It accounts for the binding of the target electron. At impact parameters greater than v/ω_f, the target electron adjusts more and more adiabatically to the

slow varying external field, and the function g tends asymptotically towards 0. For impact parameters smaller than $0.5v/\omega_f$, g is practically equal to 1.

The next step of the calculation in ref. [36] is to extract the energy transfer $T_{at}(b)$ in a collision with an atom at impact parameter b. The authors show that one has simply:

$$T_{at}(b) = \int d\vec{r} T(b_e) \rho_e(\vec{r}) , \qquad (14)$$

where $\rho_e(\vec{r})$ is the electronic density at point $\vec{r}$ with respect to the target nucleus. The integral in (15) is calculated numerically.

In the same way, one can calculate the contribution of core target electrons to the energy loss of a channeled ion, at a given point of the transverse plane, considering the core electrons associated to the strings delimiting an axial channel (see Fig. 4). Such a calculation has been performed in the frame of the classical oscillator approximation (case of swift heavy ions with $\kappa > 1$) in ref.[39], and a similar analysis is available in ref. [7]. In both papers the target was a Si crystal and only well-channeled ions were considered. The accessible transverse space of these ions was outside the shell radius of the target core-electrons and thus the value of the function h in relation (13) was equal to 1.

The authors of refs [7,39] have also evaluated the contribution to slowing down due to the valence or conduction electrons, of mean density $\overline{\rho}_g$. This quasi-free Fermi gas can be characterized by the plasma frequency

$$\omega_p = \left(4\pi \overline{\rho}_g e^2 / m_e\right)^{1/2} . \qquad (15)$$

ω_p is of the order of 10 eV, and, for swift ions, the associated adiabatic cut-off parameter v/ω_p is very large, much higher than the radius r_0 of a unit cell in the transverse plane. In such a situation the treatment used for the evaluation of the core electron contribution cannot be applied. It would concern a much too large number of electrons and, moreover, at large distances from the ion, one cannot anymore describe the slowing down in terms of individual binary collisions. Then, in ref. [7,39] the authors have divided the energy losses in two fractions, corresponding respectively to close and distant collisions. The first part is due to energy transfers to the valence electrons inside the unit shell radius, inside the channel where the ion lies. The corresponding energy loss was obtained by integration, over the impact parameters with respect to the ions, of transfers T_{sudden} to free electrons, with a weight given by the local electron density. The contribution of more distant collisions, at impact parameters greater than r_0 (the radius of the unit cell, in the transverse plane, that is associated to a string of atoms) was obtained *via* relation (11) in which b_{min} was replaced by r_0 and b_{max} by the adiabatic cut-off impact parameter corresponding to a frequency $\langle\omega\rangle = \omega_p$.

We now come back to the assimilation of the ions to point charges. This assimilation becomes questionable when the shell radius of the electrons that remain attached to the ion are no more small at the scale of the impact parameters involved in the collisions leading to the slowing down. This is an important effect at moderate velocities. Usually, the ion size is taken into account by introducing an effective charge Z_1^* instead of the real charge Q in expressions giving energy transfers or stopping powers, like the relations (11) to (13). The problem of the screening of non-fully stripped projectiles has been recently addressed in ref. [40,41]. We will see in subsection IV 2 that, at a given velocity, the mean charge-state of channeled ions may markedly differ from the equilibrium charge-state in random media. This must of course be taken into account when analyzing energy losses in channeling.

We finally address the question of energy loss fluctuations ("energy straggling"). Energy loss is a stochastic process. Let us consider an ion with a given charge-state Q. As already pointed out, the energy loss of this ion can be divided in two parts. The first one arises from distant collisions; it can be considered as a continuous slowing down, and its contribution to energy straggling can be neglected. The second one, related to individual binary collisions is usually the main cause of energy straggling. In a binary collision model, the number of energy transfer events for a given path δx in matter is a random variable, and so is the energy transferred in each collision. Thus there is an energy loss distribution, the mean value of which defines the stopping power S through $<\delta E> = S\ \delta x$. If the width of this distribution is large with respect to the maximum energy transfer in one single interaction, the distribution tends towards a gaussian, the width of which is associated to a variance $\delta\Omega^2$. In random media, the upper limit of $\delta\Omega^2$ has been estimated by Bohr [20]. It applies to ions of velocity larger than the orbital velocity of all target electrons. Introducing corrective factors due to relativistic effects one gets the relation:

$$\delta\Omega^2 = 4\pi\, Q^2 e^4 \rho_e \delta x \gamma^2 X = \delta\Omega_B^2 \gamma^2 X \qquad (16)$$

where $\delta\Omega_B^2$ is the non-relativistic Bohr result, γ the Lorentz factor, and X a correction factor due to the departure from the Rutherford scattering law at relativistic energies [34].

For lower ion energies two effects should be considered. First, as seen above, there is a definite lowering of energy transfers to tightly bound electrons, which can be taken into account by introducing a reduced value of ρ_e in relation (16). This effect, that tends to lower $\delta\Omega^2$, is somewhat compensated by effects related to charge exchange, that plays a major role for heavy ions at high and intermediate velocities. The mean charge-state of such ions in matter fluctuates around a mean value, which has two consequences on energy loss processes. First, to each charge value is associated a given stopping power value (see relations (11) and (12)). Second, any charge exchange process involves an energy transfer. For these two reasons, the charge state fluctuations introduce energy loss fluctuations that have been recently shown to be dominant, when compared to the values obtained by relation (16), for slightly relativistic heavy ions in low Z targets [42].

We now come to the case of channeled ions. We have seen that, in channeling geometry, the very broad energy loss distribution is associated to the transverse energy distribution: it does in no way reflect the energy loss fluctuations of a given ion. Such fluctuations are reflected in the energy loss distribution of ions of given $E_\perp$. We consider here the case where these ions have a long enough path to explore uniformly their available accessible transverse space $A(E_\perp)$. The variation of energy losses that may occur along the ion trajectories during this exploration will be considered in the next subsection. We have seen that the energy straggling given by relation (16) is due to close collisions. In order to estimate its value for a well-channeled ion with low $E_\perp$, one must then introduce in relation (16) a value of ρ_e equal to the mean electron density sampled by this ion in its accessible transverse space $A(E_\perp)$. As ρ_e is much smaller than the average electron density in the solid, the value of $\delta\Omega^2$ is strongly reduced. Also, we will see in subsection IV 2 that the dominant charge exchange processes take place in the vicinity of nuclei, and are thus suppressed for well channeled ions that are confined near channel centers. As a consequence, these ions will also be less submitted to energy loss fluctuations in connection with charge exchange. The general conclusion is thus that ions with low and well-defined $E_\perp$ experience energy loss fluctuations much lower than random ions.

1.b Impact parameter dependence of stopping rate: measurements.

The first systematic study of the variation of energy loss with the transverse energy $E_\perp$, and thus the accessible transverse space $A(E_\perp)$ of an ion has been achieved by Datz et al. [10], in planar channeling experiments. Planar channeled ions oscillate between two adjacent atomic planes. The planar potential is non-harmonic, and thus the wavelength associated to the oscillations depends on the oscillation amplitude, which, of course, increases with $E_\perp$. This feature was used in ref [10] in transmission type experiments through thin gold crystals. The incident beam was sent parallel to the (111) plane. A very collimated detector was used to receive only the ions leaving the crystal precisely along the incident direction, and to analyze their energy. These ions have necessarily undergone an integer number n_i of half-oscillations inside the planar channel. To each value of n_i corresponds a distinct and narrow $E_\perp$ window. The registered energy loss spectrum thus consists in distinct peaks, the positions of which provide the stopping rate values associated to the set of selected $E_{\perp i}$. These values are averaged over a half-oscillation, i.e. over the accessible $A(E_{\perp i})$. Inside this area, the local energy loss rate may vary considerably, in connection with the local variations of the electronic density, especially if the ion has a high $E_\perp$. The experiments of ref. [10] can provide estimates of the local value of the stopping power, at given distance from an atomic plane, when comparing the losses suffered by ions having respectively undergone n_i and $n_{(i+1)}$ half-oscillations. This comparison gives the stopping rate in the region between $A(E_{\perp i})$ and $A(E_{\perp (i+1)})$.

A measurement of the local stopping rate very close to atomic strings has been performed by Vickridge et al. [43]. In this work, the excitation curve (yield as a function of incident beam energy) of the very narrow and quasi-isolated resonance of the nuclear reaction $^{27}Al(p,\gamma)^{28}Si$ has been registered, by scanning the proton beam around the resonance energy (992 keV), in random and axial alignment geometry on an Al crystal. In channeling, only the ions entering the crystal at distances from the strings of the order of the thermal vibration amplitude of the Al atoms (about 0.1 Å), can induce the reaction. Moreover, the reaction can take place only near the surface, in the small fraction Δx of the ion's path during which they remain at such small distances from the strings, i.e. before the shadow cone radius becomes too large. The thick Al crystal thus behaves as a thin target and the excitation curve consists in a narrow peak. The integral of the peak is fixed by the value of Δx. However, at given integral, the height and width of this peak are determined by the local stopping power, i.e. by the number of atomic collisions required to loose an energy amount equal to the resonance width. The higher the stopping rate, the smaller the peak height and the larger the peak width. For the 1 MeV protons used in ref. [43] it was found that the local electronic stopping very close to the strings was an order of magnitude larger than the random stopping.

In subsection IV-4, we will give examples of stopping rate measurements for ions remaining at very large impact parameters from atomic strings, of the order of r_0 (hyperchanneled ions).

2 Charge exchange

Let us first start this section with some semantical notions, in order to clarify the various processes that will be discussed therein.

Ion ionization may occur by impact on a target nucleus (Nuclear Impact Ionization, NII) or on a target electron (Electron Impact Ionization, EII). At high energies, ionization cross sections roughly scale as the square of the target charge, and thus NII cross sections are generally much higher than EII ones, except for very light targets. This is also true for inner-

shell excitation of the projectile (Nuclear Impact Excitation, NIE, and Electron Impact Excitation, EIE).

At high velocity, electron transfer from a target atom into a bound state of a projectile ion restricts to a three – body process. Energy and momentum conservation may involve the recoil of the target atom. We will refer to this process as the Mechanical Electron Capture (MEC). Alternatively, the excess energy and momentum corresponding to the electron capture can be carried out by a photon. This process is called radiative recombination when the initial state corresponds to a free electron, and Radiative Electron Capture (REC) for an initially bound electron. Radiative recombination is the time reverse process of the photoelectric effect. In a third mechanism, electron capture can be resonant when the energy of the transition between the initial and final state of the electron matches the energy of an electronic excitation of the ion. This resonant capture process is called Dielectronic Recombination (DR) for an initially free electron and Resonant Transfer and Excitation (RTE) for a bound target electron. Dielectronic recombination is the time reverse of the Auger emission. RTE and DR can occur only at given resonant projectile energies, and for given initial electronic configurations (in particular it is forbidden for bare ions).

NII and MEC are generally the dominant charge exchange processes between a swift heavy ion and an atomic target (except for highly relativistic ions, and/or very low Z_2 values of the target atoms). As ions penetrate inside a target, their electronic configurations evolve until ionization and capture probabilities level, leading to charge equilibrium after penetration through a given target thickness. Fluctuations in the balance between capture and loss events lead to a charge state distribution around the equilibrium charge. At equilibrium, the occupancy of an electronic shell with principal quantum number *n* is mainly characterized by the adiabaticity parameter $\eta_n = v_{ion}/v_n$, v_n being the average electron velocity in a projectile bound state, and v_{ion} the ion velocity. As predicted by Bohr, if $\eta_n < 1$, the n-shell is filled, and if $\eta_n > 1$, it is empty. To a lesser extent the equilibrium charge depends also on the atomic number of the target atoms.

NII and MEC involve the interaction of the projectile with the screened nuclear target Coulomb field, and are restricted to impact parameters of the order of the orbital radius of the electron in the bound state of the projectile.

As a consequence, for fast ions in channeling conditions, NII and MEC will be strongly suppressed because the non-uniform flux distribution inside the crystal favors large impact parameters. Also, this non-uniform flux allows one to study the impact parameter dependence of NII and MEC. This can be done over an impact parameter range extending from the rms. amplitude of the target atom thermal vibrations up to the maximum distance of approach to atomic strings or planes at which these processes may occur. In particular, studying MEC as a function of impact parameter is particularly attractive at low values of η_n, as we will see below.

Then, for well-channeled ions, ionization will occur through electron impact and capture will require the emission of a photon (REC), except at suitable energies for which the resonant RTE processes is allowed. As illustrated by the electron density map in Fig. 4-b, ions with the lowest transverse energies sense only very low electron densities. For instance, hyperchanneled ions (e.g. those that are confined inside equipotential 3 of Fig. 4-a) sample in the average a density of ~0.1 e-Å^{-3}, which is 7 times smaller than the mean electron density in silicon. Moreover, this density arises only from quasi-free electrons of the valence or conduction bands. They will be characterized by a much narrower momentum distribution (Compton profile) than core electrons, located close to the atomic strings (typically inside contour 5 of Fig. 4-b).

One can act on the electron density sensed by channeled ions by varying their associated transverse energy distribution. This can be done by slightly tilting the crystal, by angle $\delta\Psi < \psi_C$, thus by introducing a small misalignment between the crystal axis and the beam incidence. If the initial incidence was parallel to the axis, this misalignment will induce an increase by $E\delta\Psi^2$ of the transverse energy of channeled ions, that will enlarge their accessible transverse space, and accordingly the "electron target thickness". One can see in Fig.4-b, when comparing contours close to the channel center and close to the atomic strings, that a tilt angle smaller than the channeling critical angle can lead to an enhancement by about one order of magnitude of the electron target thickness sampled by the best channeled ions.

We will now illustrate how this ability of channeled ions to experience a dense, non uniform electron target, can lead to original results on charge exchange

3 Combined energy loss and charge exchange measurements

The effect of channeling on the charge state distribution at the exit of a crystal target is the most dramatic when incident ions are very far from the charge at equilibrium. In this situation, one can access to exclusive information on ion-matter interaction, as we will see now.

3.1 $E_\perp$ selection: measurement of EII cross-sections and of hyperchanneled ions stopping

Fig. 18 presents the charge state distributions $F(Q_{out})$ obtained with 27 MeV/u Xe^{35+} incident ions (i.e. with 19 electrons) on a 20.7 μm thick silicon crystal target [12]. In this experiment, η_L = 1.2, and the charge at equilibrium in random conditions corresponds to a partly empty L-shell, as illustrated by the charge distribution $F_R(Q_{out})$ associated to ions having crossed the crystal upon a random orientation. This charge distribution is centered around Q_{out}=50, i.e. is far from the incident charge state. For <110> axial alignment, the charge state distribution $F_C(Q_{out})$ ranges from Q_{out}=35 up to Q_{out}=53. Actually, this distribution reflects the transverse energy distribution of channeled ions: ions with a high transverse energy experience all impact parameters, and their charge at the exit is close to the random equilibrium charge. For such ions, as well as for a random orientation, the balance between NII and MEC determines the charge distribution. On the other side, ions with the lowest transverse energy experience regions where the electronic density is very small. However, one can observe only a very small fraction of ions frozen in their initial charge state. This means that, even for channeled ions, for which NII is forbidden, ionization events by electron impact may occur. In Fig. 19 is shown the dependence of $F_C(Q_{out}=37)$ (nearly frozen ions) on the crystal orientation relative to the axial direction. As a comparison the Ly_α yield is also shown. Ly_α emission results from K-shell excitation or ionization, which is only possible by nuclear impact (the kinetic energy is below the threshold for K-shell EII). Thus the Ly_α dip reflects the close collision extinction dip. It can be deduced from Fig. 19 that the critical transverse energy to emerge with Q_{out}=37 is 5.6×10^{-3} times smaller than the critical channeling transverse energy given by eqs. 4-5. Thus these ions are hyperchanneled. With the help of simulations, the mean transverse energy corresponding to each charge state was determined, together with the mean sampled electron density. These correspondences are shown in Fig. 20. The EII cross-sections were evaluated for each charge state, as well as the impact parameter dependence of energy loss. For the best-channeled ions, the latter was found to be only slightly dependent on the local electron density. In other words, the energy loss at large distance from the atomic strings is dominated by distant collisions with the valence electron gas.

3.2 Emission of target electrons

Information on the impact parameter dependence of target ionization has been obtained recently by our collaboration group, in a similar study with 29 MeV/u Pb^{56+} ions incident on a thin silicon crystal (1.1μm). Again the exit charge-state was used to discriminate over ions with different transverse energies. The energy loss was measured with a high resolution, and the secondary electron emission from both entrance and exit target surfaces for each ion impact was measured (electron multiplicities). As in the previous example, for <110> axial orientation the charge state distribution at emergence, shown in Fig. 21, is very broad, reflecting the transverse energy distribution. It ranges from Q_{out}=56 up to Q_{out}=78, whereas the random charge distribution is centered around Q_{out}=69. Fig. 22 shows various electron multiplicity distributions from entrance and exit target surfaces, together with energy loss distributions. These distributions correspond to different emerging charge states associated respectively to well channeled ions frozen in their initial charge state (Q_{out}=56, Fig. 22-a), and poorly channeled ions (Q_{out}=72, Fig. 22-b) in axial channeling conditions. The distributions obtained for random incidence, and corresponding to Q_{out}=72 are also displayed in Fig. 22-b. As already mentioned in subsection IV-1, we show in this figure reduced energy loss values ΔE_{red}, in units of mean random loss ΔE_R, with a first order correction accounting for the mean ion charge state in the target: $\Delta E_{red} = \Delta E(Q_{out}) \times (2\langle Q\rangle_R^2/(Q_{in}^2+Q_{out}^2)/\Delta E_R$, where $\langle Q\rangle_R$ is the mean random charge state inside the target and Q_{in}=56. Well-channeled frozen ions emerge from the crystal with a mean reduced energy loss of about 0.5. From Fig. 21 they represent typically half of the total beam. In the energy loss distribution corresponding to the <110> orientation, one can select the ions having lost the minimal energy (see the inset on the top left of Fig. 22-a). This very small fraction (about 0.5% of the total beam) has a reduced energy loss lower than 0.37. These ions are hyperchanneled. For poorly channeled ions, (Fig. 22-b) the situation is completely different: such ions enter close to the atomic strings and thus their energy loss is strongly enhanced close to the entrance. Once the atomic string repels them, their energy loss rate is reduced, until they approach again another string. As the crystal is thin, statistical equilibrium is not fully established at the exit. In the ion path, the number of close collisions with strings, during which the energy loss rate is very high, is small (typically between 1 and 4**)**. It may exhibit strong relative variations when comparing the trajectories of two ions with very similar $E_\perp$ The resulting energy spectrum is very broad, and its mean value is much higher than the random loss. One can see in Fig. 22-b that the maximum reduced losses measured extend up to 2.5. Although the target thickness is much larger than the path needed to reach the center of the channel for ions entering close to a string (about 2000Å), high transverse energy ions may experience very large integrated electron densities.

Electrons collected from the surfaces are mainly low energy secondary electrons. The corresponding electron yield is correlated to energy loss, as illustrated in Fig. 22 for both backward and forward emissions. The backward yield for the best channeled 56+ ions is attenuated by a factor 0.6 with respect to the random yield. The same behavior is observed for the forward emission yield of these ions. In this latter case, as in random geometry the ions emerge with a higher charge-state than the frozen 56+ well-channeled ions, the comparison was achieved after correction for the Q^2 dependence on the ion-electron collision cross-sections. The local electron density sampled by a hyperchanneled ion in the <110> axis is less than 15% of the average electron density of silicon, a reduction much stronger than the attenuation of the electron multiplicity for these ions. The attenuation of energy loss, which is due mainly to the extinction of close collisions near the channel center, is also much more

pronounced. This shows that distant collisions are the main source for secondary electron emission by hyperchanneled projectiles.

For poorly channeled ions, one observes an enhancement by a factor of 2 of the backward electron multiplicity compared to random conditions. The maximum of the forward electron yield distribution is the same as in random condition, with a tail extending towards large values. Ions with a high transverse energy may leave the crystal at any position in the transverse space, as in random conditions. Some ions may undergo close collisions along a string in the vicinity of the exit, which leads to the tail observed towards high forward electron multiplicities.

To conclude, electron multiplicities can be used to identify clearly the entrance impact parameter of channeled ions. It was deduced from these experiments that the forward electron multiplicities are not only the result of ionization events near the crystal exit, but may also arise from highly ionizing events, in relation with glancing collisions with strings, much deeper in the crystal. Thus the forward electron yield carries less information about the conditions of emergence than backward emission does about entrance conditions.

3.3 Local longitudinal momentum distribution of target electrons

Local target-electron momentum distribution can also be inferred from charge exchange measurements in channeling. For KLL Dielectronic Recombination for instance, the resonance condition is (non relativistic) $\left((m_e/M_{ion})\vec{p}_{ion} - \vec{p}_e\right)^2/2m_e = E_K - 2E_L$, where $\vec{p}_{ion}$ and $\vec{p}_e$ are respectively the ion and electron momenta in the laboratory frame, E_K the initial K-shell binding energy, and E_L the L-shell binding energy in the final state. Thus the DR resonance profile is broadened by the longitudinal momentum distribution of the electron to be captured. Andersen et al. [39] have shown that the KLL DR resonance profile depends on the energy loss rate of channeled Br^{33+} ions in a 1 μm thick <110> Si crystal. Fig. 23 shows their data for the capture rate as a function of incident ion energy, for 3 adjacent energy loss windows, ranging between 0.41 and 0.62 times the random energy loss rate. Such ions sense mainly valence electrons of silicon. Both amplitude and width of the resonance are found to vary with the energy loss. The amplitude is directly proportional to the electron density, whereas the width depends on the electron Compton profile. Assuming that valence electrons behave locally like a Fermi electron gas, energy loss rates, DR amplitudes and the evolution of the resonance width could be reproduced quantitatively.

A detailed analysis of the target electron Compton profile was made by Andriamonje et al.[8], by observing REC photons. In the same way than a DR resonance is broadened, the energy of REC photons is spread by the longitudinal target electron momentum distribution. In the projectile frame, a target electron has a kinetic energy E_c, and the energy of a photon associated to the capture of an electron of initial binding energy E_i and longitudinal momentum p_z into the n-shell of the projectile is

$$h\nu_{n-REC} = E_c + E_n - \gamma E_i - \beta\gamma p_z c, \qquad (17)$$

where E_n is the binding energy of the n-shell. Fig. 24 shows two X-ray spectra obtained with 60 MeV/u bare krypton ions incident on a 37μm thick silicon crystal. K- and L-REC peaks are observed for both random and <110> axial orientation conditions. At such a high energy, the mean charge-state at equilibrium corresponds to bare ions, so that REC was observable for both random and channeling conditions in this experiment. For a random orientation, all target electrons of silicon contribute with the same weight to REC. The calculated contributions from core electrons (K and L-shells of silicon) and valence electrons, that have a

narrower Compton profile, are drawn on the spectra. For <110> axial orientation, the core electron contribution drops down by one order of magnitude, whereas the valence electron contribution is only slightly reduced. By varying the crystal tilt angle from axial to random orientation, the authors of ref.[8] could follow and interpret the evolution of both components. In particular impact parameter dependent Compton profiles for core electrons were required to reproduce the shape of the REC peaks at small tilting angles, i.e. when the ion flux distributions are non-uniform. Such a local information is not available by other techniques investigating Compton profiles, because they integrate uniformly over all impact parameters.

3.4 Deceleration of highly charged ions

We have seen that channeled ions have a reduced probability to undergo charge exchange, due, first, to their large impact parameters relative to the target nuclei and, second, to the reduced electron density far from the atomic planes and rows. One may use this property to decelerate highly charged ions (for instance bare or hydrogenic uranium ions) down to low energies where they are very far from charge equilibrium in random conditions, although the capture cross-sections increase dramatically with decreasing energy. The idea is that the very high charge of those slow ions may lead to extremely high energy-loss rates, despite the very low electron density encountered. There are three main limitations for deceleration of ions frozen in a high charge-state. The first one is related to the increase of transverse energy due to electronic multiple scattering (dechanneling). The second one is the increasing MEC probability at very large impact parameters: capture into highly excited states occurs when the projectile velocity is of the same order than the corresponding orbital velocity. The last limitation is due to the high probability of capture by REC in very thick targets: even if the electron density is very low at the center of a crystal channel, one must account for the strong increase of REC cross-sections at low energies. We now discuss the extent of these limitations.

Concerning the first point, the mean increase $\Delta E_\perp$ of transverse energy due to the scattering of channeled ions on target electrons can be estimated as a function of the total energy loss ΔE:

$$\Delta E_\perp = \frac{1}{2}\frac{m_e}{M_{ion}}\Delta E \,. \qquad (18)$$

The factor 1/2 in Eq. (18) accounts for the fact that only close ion-electron collisions contribute to angular scattering. However, this close collision contribution drops down severely for very well channeled ions. As already stated in subsection IV3.1 when discussing the results of ref. [12], the energy loss of hyperchanneled ions is essentially due to distant collisions, which do not lead to appreciable angular deflections. Thus Eq. (18) may overestimate considerably the increase of transverse energy for hyperchanneled ions. Note also, but this is a second order effect, that for a given accessible transverse space, the reduction of the overall ion energy counteracts the spreading of the angular distribution ($\Psi_{max} = (E_\perp / E)^{1/2}$).

About the second point, channeled ions may avoid MEC as far as the Rydberg ion formed by a capture into a highly excited state has a much smaller size than that of the crystal channel (i.e. the radius should not exceed 0.5 Å). In such a situation MEC is avoided for a well-channeled ion (remaining near the channel center) as there is no possible contribution of the target nucleus to an electron capture. Using the hydrogenic atom model of Bohr, one finds that the orbital velocity for a shell radius of 0.5 Å in a uranium atom is roughly $10v_0$. (it

corresponds to a principal quantum number n = 10). This is the velocity of a uranium ion at 2.5 MeV/u. It is then hopeless to slow-down a H-like uranium ion in a crystal below this energy, but it is certainly worthwhile to try to obtain hydrogenic uranium ions at such low energies. One is also helped in this task by the fact that, even for well-channeled ions, electrons captured in highly- excited states have a strong probability to be lost through EII. Classical Transport Monte Carlo simulations have been undertaken recently by F.Grüner *et al*. [44] in the MeV/u energy region, that describe this competition between capture and ionization as a function of impact parameter in this intermediate velocity regime. We will come back on this point in the next section.

For the third point, concerning the probability of REC by hyperchanneled ions, a theoretical estimate is easier. REC cross-sections have maximum values for capture into the lower n states of the projectile, and thus REC can be treated as a local process. Actually, REC cross sections are limited to less than 10^4 barns per electron for very heavy ions in the energy range described above (more than 2.5 MeV/u). Then, the survival probability for well channeled ions, sampling electron densities of about 0.1 $e^{-}Å^{-3}$, is non zero up to lengths of a few ten microns. This allows to decelerate considerably highly charged ions.

A first attempt has been performed at GSI with 20 MeV/u U^{91+} ions extracted from the ESR storage ring [45]. After a path length of 11 μm of silicon (<110> alignment) nearly 30% of the incident ions remained frozen in their incident charge, and their energy loss was 4% of the initial energy, whereas the random energy loss rate was 5%. Starting from this result, Fig. 25 shows how the energy loss rate should evolve with energy for well-channeled U^{91+} ions. Since these ions do not capture electrons, the energy loss rate should continue to grow up like $1/v^2$ with decreasing energies. Below 15 MeV/u, we arrive at the paradoxical situation where channeled ions loose more energy than unchanneled ions, in relation with the Q^2 dependence of the stopping power. A recent and unpublished study with a thicker crystal and a lower incident energy confirmed this effect.

4 Breaking the reversibility rule: transverse cooling and heating

Recently, Assmann *et al.* [19] reported a violation of the channeling-blocking reversibility rule described in section II. This rule predicts in particular that an initially uniform angular distribution of ions should retain its uniformity when the ions cross a crystal. The authors of ref. [19] have sent various beams, with uniform distributions over an angular range very large at the scale of channeling critical angles, on various crystals, and they observed strong anisotropies in the emerging beam. In some cases an enhancement of the angular distribution can be observed along crystallographic axes or planes (transverse cooling), in other cases transverse heating leads to a depopulation in these directions. Both heating and cooling phenomena depend on the ion velocity, on the projectile and target nuclear charges, and on the considered crystallographic direction. In particular, cooling to heating transitions occur when the energy of the beam of a given species decreases. Fig. 26 illustrates such a situation for Y ions transmitted through a 3.4 μm thick Si crystal [46]. The authors proposed that the dependence of charge exchange with impact parameter could explain the phenomenon, at least partially. Consider, for instance, an ion of charge Q and transverse energy $E_\perp$, given by Eq. (3). Its transverse motion is governed by a string potential per unit charge U(r), which is a decreasing function of r. If a charge-changing event (single electron capture or loss) occurs at distance r, the transverse energy of the ion varies by $\pm$ U(r), and, in the mean time, the potential barrier associated to dechanneling varies by $\pm$ U(r_{min}), r_{min} being a typical minimum distance of approach to atomic strings or rows of the order of ρ. As U(r_{min})≥ U(r), an electron loss leads to transverse cooling, while an electron capture leads to transverse heating. When charge equilibrium is reached the same number of ionizations and

captures occur in the average. Let us then consider the situation of an ion experiencing a cycle consisting of an equal number n of capture and loss events. As the charge of the ion is conserved after the cycle, so is the potential barrier $Q.U(r_{min})$. Let us now call respectively r_C and r_L the average radii associated to a capture and a loss event. The cycle will induce a change of the transverse energy of the ion whose absolute value is equal to $n(U(r_L)-U(r_C))$. Thus, if $r_C < r_L$, the cycle will induce transverse cooling and, conversely, if $r_C > r_L$, it will induce transverse heating. The overall heating or cooling efficiency is high if r_C and r_I differ significantly, and, of course, if the charge-changing cross sections are large, which is the case for heavy ions at intermediate velocities. A few additional remarks are needed:
- in the experiments where cooling or heating patterns have been observed [19,44,46], charge exchange cross sections are huge, and capture and loss processes take place at large impact parameters. In particular, capture occurs into excited states of the projectile, which may lead to a delayed auto-ionization, at large distance from the strings or planes. This could explain that cooling is more persistent along the major axial directions.
- a full theoretical description of the phenomenon has been undertaken [44] by means of n-body Classical Transport Monte Carlo, which leads to encouraging results.

V Resonant Coherent Excitation.

Okorokov [47] predicted in 1965 that channeled particles should be sensitive to the periodicity of the charge distribution along crystallographic directions, i.e. to harmonics of the string potential, $U(\vec{r},z)$, the variation of which with z is now considered. The zero-order continuum potential is obtained after averaging, through Eq. (1), over all the atoms of a string. Higher order terms correspond to the maxima of the Fourier transform of $U(\vec{r},z)$. Resonant Coherent Excitation (RCE) can occur when an excitation frequency $\Delta E/h$ of the projectile matches a harmonic of the collision frequency along an atomic string:

$$\frac{\Delta E}{h} = k\gamma\frac{v}{d} \qquad (19)$$

where v is the projectile velocity, d the interatomic spacing along the propagation direction, γ the Lorenz factor and k a positive integer. In other words, RCE is the resonant absorption (or emission) by the projectile of a momentum corresponding to the reciprocal lattice vector $G_k = k\,2\pi\hbar/d$.

Under planar channeling conditions, one may adjust the excitation frequency by varying the angle θ relative to the atomic strings belonging to the plane [49]. For instance in the case of the (100) plane of a fcc crystal, Eq. (19) becomes

$$\frac{\Delta E}{h} = \gamma\frac{v}{d_{\langle 100\rangle}}\left(k\cos\theta + l\sin\theta\right) \qquad (20)$$

where $d_{\langle 110\rangle}$ is the interatomic distance along a <100> string, θ the angle between the trajectory and the <100> axial direction, and k, l are positive integers.

The first observation of atomic RCE has been reported by Datz *et al.* in refs. [48] and [13]. The authors measured the ionization probability as a function of incident energy for axially channeled H-like, low-Z ions (Z=4-9). When the incidence energy matches one of the harmonic resonance defined by eq. (19) for n=1 to n=2 electronic excitation, the frozen H-like fraction of emerging ions drops down, in connection with the higher ionization probability of the n=2 states. During these experiments, energy shifts and broadening of resonances

compared to vacuum energy transitions have been observed, and interpreted in terms of influence of the static crystal field and of the wake field, the latter corresponding to the polarization of the electron gas in the vicinity of the moving charge. Further complementary studies have been performed since then. Datz *et al.* did observe atomic RCE through the radiative decay of the excited state [14]. Komaki *et al.* have extended these measurements to higher Z ions at higher energies [15]. By recording simultaneously the energy loss, they could obtain detailed information on the Stark splitting of the n=2 state of Ar^{17+} ions as a function of the impact parameter in planar channeling conditions. Actually, the static transverse electric field sampled by an ion in the vicinity of an atomic plane (or row) is responsible for this Stark splitting. The stronger the electric field, the stronger the splitting. Low transverse energy ions, which can be selected through the weak energy loss they experience, are confined in regions where the transverse field is small, and the resonance energy is thus closer to its value in non-perturbed condition. On the opposite, ions with the highest transverse energy, which can be selected through the strong energy loss they experience, have an accessible transverse space extending nearly all over the channels. They can thus undergo RCE both close to the channel walls, with a high efficiency, in regions where the Stark splitting is strong, and at larger distances, with lower efficiency, in regions where the Stark splitting is weak. The consequence is that the energy width of the resonance is significantly broadened for these ions.

Note that not only the RCE probability is enhanced close to the strings or planes, but also the ionization of the excited ion, which makes the quantitative evaluation of the RCE process not straightforward. Also, as RCE takes place preferentially close to atomic strings, the influence of target atoms thermal vibrations cannot be ignored, as it is done for instance in relation (1) where all the atoms are assumed to be perfectly aligned along a string. The potential $U(\vec{r},z)$ is thus a random function, with a given taking for each ion. Such takings can be calculated by summing the contribution to $U(\vec{r},z)$, of the individual atoms of a string placed at random distances from regular lattice sites, according to the thermal vibration amplitude distribution. These fluctuations tend to lower the value of the coherence length associated to a RCE resonance, and thus contribute to a broadening and a weakening of the resonance.

So far, nuclear RCE has not been observed, but theoretical descriptions and predictions on this effect are available [16].

VI Concluding remarks.

We have tried to show that the understanding of ion motion in crystals raises important questions related to ion-matter interactions. The introduction of the continuum model by Lindhard [1] has allowed a description of channeling phenomena at a high level of generality. It has in particular permitted to benefit of powerful concepts originating from statistical physics. Setting the limits of the continuum description, in connection with atomic periodicity along crystallographic directions or with non correlated or poorly correlated scattering events, was also a task of fundamental importance. Once understood, channeling effects provide, in turn, unique opportunities for refined studies of ion-matter interaction. These opportunities are mostly related to the very non-uniform ion flux that develops inside crystals in aligned geometry. This feature can be taken into benefit in order to determine precisely the impact parameter dependence of various processes. As moreover the ion flux is focused far from atomic strings or planes, one can study very specific aspects of ion-electron interactions without being perturbed by the interactions with target nuclei. We have given a few examples of such studies in section IV. Of course, many other studies would have deserved a detailed description. In particular, we have not shown how one could also take into benefit the absence

of interactions with target nuclei to study unexplored events, with extremely low associated cross-sections. Let us only mention in this domain the study of the resonant trielectronic recombination, a process in which the capture of an electron promotes two other electrons, already bound, into excited states. Channeling measurements have allowed to set for the cross-section of such a process a lower limit two orders of magnitude weaker than previously reported during ion-gas experiments [50]. In the same spirit, channeling experiments are planned in order to evidence a process called nuclear excitation by electron capture and to determine its cross-section. This effect, resonant with the ion beam energy, in which the capture of an electron in an atomic shell leads to nuclear excitation, is the reverse of internal conversion [51].

We have also illustrated applications of channeling for lattice site determination, and shown that these applications could interest domains as different as material science and nuclear physics. In what concerns material and surface science many other and very powerful techniques are available. X-rays or electron diffraction for instance take benefit of the very high amount of information that can be derived from measurements in reciprocal space. Scanning tunnel or atomic force microscopy may provide atomic resolution and allow to study objects of very small lateral dimension. The specificity of channeling measurements is related to two main features. First, these measurements probably present the highest sensitivity to atomic displacements (down to 10^{-2} Å!). Second, they illustrate in a quite straightforward way the presence of effects implying coherent atomic displacements, such as lattice strain or surface relaxation. However, even if these effects are easily detectable, the refined analysis of the measurements requires some effort (computer simulation are often needed) and a real knowledge and understanding of channeling.

Another application that would have deserved presentation is the ability to deflect high-energy beams using bent crystals. The bending is such that the change in the crystalline orientation is kept significantly smaller than the channeling critical angle over a length corresponding to the oscillation of an ion in a channel. Then, ions may remain channeled and guided by the continuum potential. Experiments have been performed at CERN with light [52] and heavy ions [53] in the relativistic energy range (above 100 GeV/nucleon). These experiments have shown that, after transmission through a bent crystal, a few cm long, a large fraction of the incident beam (10 to 50%) could exit, with negligible angular divergence, having been deflected by a few mrad. Dechanneling by crystalline defects, induced by crystal bending, is mainly responsible for the relatively low transmission factors. Bent crystals are now routinely used to deflect charged particle beams in high-energy accelerators.

Acknowledgements. We would like to thank all authors who allowed us to reproduce their data. A. L'Hoir and J.-C. Poizat are gratefully thanked for their very helpful criticisms and suggestions..

References

[1] J. Lindhard, Mat. Fys. Medd. Dan. Vid. Selsk. 34 (14) (1965).
[2] L.C. Feldman, J.W. Mayer et S.T. Picraux: "Material Analysis by ion channeling", Acad. Press, New York, London, Paris, San Francisco, Sao Paulo, Sydney, Tokyo, Toronto, (1982).
[3] A.F. Tulinov, Dokl. Akad. Nauk. SSSR 162 (1965) 546 (Sov. Phys.-Doklady 10 (1965) 463).
[4] J.S. Forster, I.V. Mitchell, J.U. Andersen, A.S. Jensen, E. Laegsgaard, W.M. Gibson, K. Reichelt, Nucl. Phys. A 464 (1987) 497.

[5] F. Goldenbaum, M. Morjean, J. Galin, E. Liénard, B. Lott, Y. Périer, M. Chevallier, D. Dauvergne, R. Kirsch, J.C. Poizat, J. Remillieux, C. Cohen, A. L'Hoir, G. Prévot, D. Schmaus, J. Dural, M. Toulemonde, D. Jacquet, Phys. Rev. Lett. 82 (2000) 5012.
[6] S. Andriamonje, R. Anne, N.V. de Castro Faria, M. Chevallier, C. Cohen, J. Dural, M.J. Gaillard, R. Genre, M. Hage-Ali, R. Kirsch, A. L'Hoir, B. Farizon-Mazuy, J. Mory, J. Moulin, J.C. Poizat, Y. Quéré, J. Remillieux, D. Schmaus, M. Toulemonde, Phys. Rev. Lett. 63 (1989) 1930.
[7] D. Dauvergne, C. Scheidenberger, A. L'Hoir, J-U. Andersen, S. Andriamonje, C. Bockstiegel, M. Chevallier, C. Cohen, N. Cue, S. Czajkowski, J-S. Forster, H. Geissel, H. Irnich, T. Kandler, R. Kirsch, A. Magel, P-H. Mokler, G. Munzenberg, F.Nickel, Yu.L. Pivovarov, J-C. Poizat, M-F. Politis, J. Remillieux, D. Schmaus, Th. Stohlker, T. Suzuki, M. Toulemonde, Phys. Rev. A 59 (1999) 2813.
[8] S. Andriamonje, M. Chevallier, C. Cohen, N. Cue, D. Dauvergne, J. Dural, F. Fujimoto, R. Kirsch, A. L'hoir, J.C. Poizat, Y.Quéré, J. Remillieux, C. Rohl, H. Rothard, J.P. Rozet, D. Schmaus, M. Toulemonde, D. Vernhet, Phys. Rev. A 54 (1996) 1404.
[9] S. Andriamonje, M. Chevallier, C. Cohen, N. Cue, D. Dauvergne, J. Dural, R. Genre, Y. Girard, R. Kirsch, A. L'Hoir, J.C. Poizat, Y. Quéré, J. Remillieux, D. Schmaus, M. Toulemonde, Phys. Lett. A 164 (1992) 184.
[10] S. Datz, C.D. Moak, T.S. Noggle, B.R. Appleton and H.O. Lutz, Phys. Rev. 179 (1969) 315.
[11] M.T. Robinson, Phys. Rev. 179 (1969) 327.
[12] A. L'Hoir, S. Andriamonje, R. Anne, N.V. de Castro Faria, M. Chevallier, C. Cohen, J. Dural, M.J. Gaillard, R. Genre, M. Hage-Ali, B. Farizon-Mazuy, J. Mory; J. Moulin, J.C. Poizat, Y. Quéré, J. Remillieux, D. Schmaus, M. Toulemonde, Nucl. Instr. and Meth. Phys. Res. B 48 (1990) 145.
[13] C. D. Moak, S. Datz, O. H. Crawford, H. F. Krause, P. F. Dittner, J. Gomez Del Campo, J. A. Biggerstaff, P. D. Miller, P. Hvelplund and H. Knudsen, Phys. Rev. A19 (1979) 977.
[14] S. Datz, P. F. Dittner, H. F. Krause, C. R. Vane, O. H. Crawford, J. S. Forster, G. S. Ball, W. G. Davies and J. S. Geiger, Nucl. Instr. and Meth. Phys. Res. B 100 (1995) 272.
[15] K. Komaki, T. Azuma, T. Ito, Y. Takabayashi, Y. Yamazaki, M. Sano, M. Torikoshi, A. Kitagawa, E. Takada and T. Murakami, Nucl. Instr. and Meth. Phys. Res. B 146 (1998) 19.
[16] Yu. L. Pivovarov, H. Geissel, Yu. M. Filimonov, O. E. Krivosheev and C. Scheidenberger, Nucl. Instr. and Meth. Phys. Res. B 119 (1996) 283.
[17] J.H. Barrett, Phys. Rev. B3 (1971) 1527
[18] E. Bögh and J.L. Whitton, Phys. Rev. Lett. 19 (1967) 553.
[19] W. Assmann, H. Huber, S.A. Karamian, F. Grüner, H.D. Miesques, J.U. Andersen, M. Posselt, B. Schmidt, Phys. Rev. Lett. 83 (1999) 1759.
[20] N. Bohr, K. Dan Vidensk. Selsk. Mat.-Fys. Medd. 18 (1948) No.8.
[21] S.T. Picraux et F.L. Vook: "Ion implantation in semiconductors", S. Namba éditor, p. 355, Plenum, New York (1975).
[22] C. Lallaizon, B. Lépine, S. Ababou, A. Guivarc'h, S. Députier, F. Abel, C. Cohen, J. Appl. Phys. 86 (1999) 5515.
[23] I. Stensgaard, L.C. Feldman et P.J. Silverman; Surf. Sci. 77 (1978) 513.
[24] J.W.M. Frenken et J.F. Van der Veen; Phys. Rev. Lett. 54 (1985) 134.
[25] C. Cohen, A. L'Hoir, J. Moulin, D. Schmaus, M. Sotto, J.L. Domange, J.C. Bouillard, Surf. Sci. 339 (1995) 41.
[26]Z.Y.A. Al-Tamimi, W.A. Grant, and G. Carter, Nucl. Instrum. and Meth. 209 (1983) 363.
[27] J.A. Davies, L. Eriksson, N.G.E. Johansson, I.V. Mitchell, Phys. Rev, 181 (1969) 548.

[28] F. Barrué, S. Basnary, A. Chbihi, M. Chevallier, C. Cohen, D. Dauvergne, H. Ellmer, J. Frankland, D. Jacquet, R. Kirsch, P. Lautesse, A. L'Hoir, M. Morjean, J.C. Poizat, C. Ray, M. Toulemonde, Nucl. Instrum. and Meth. B 193 (2002) 852.
[29] J.U. Andersen et al., K. Dan. Vidensk. Selsk. Mat. Fys. Medd. 40 (1980) 7.
[30] S.A. Karamian, J.S. Forster, J.U. Andersen, W. Assmann, C. Broude, J. Chevallier, J.S. Geiger, F. Grüner, V.A. Khodyrev, F. Malaguti and A. Uguzzoni, Eur. Phys. J. A17 (2003) 49.
[31] D.J. Hinde, Nucl. Phys. A 553 (1993) 255c.
[32] H. Bethe, Z. Phys. 76 (1930) 293.
[33] S. P. Ahlen, Rev. Mod. Phys. 52 (1980) 121.
[34] J. Lindhard and A.H. Sørensen, Phys. Rev. A53 (1996) 2443.
[35] J. F. Ziegler, J. P. Biersack and U. Littmark, "*The Stopping and Range of Ions in Solids*", Pergamon Press, New York, 1985.
[36] G. Schiwietz and P.L. Grande, Nucl. Instrum. and Meth. B 153 (1999) 1.
[37] F. Bloch, Ann. Physik. 16 (1933) 285.
[38] J. D. Jackson, *Classical Electrodynamics*, (Wiley, New York, 1975).
[39] J.U. Andersen, J. Chevallier, G.C. Ball, W.G. Davies, J.S. Forster, J.S. Geiger, J.A. Davies, H. Geissel and E.P. Kanter, Phys. Rev. A54 (1996) 624.
[40] G. Dze M. Azevedo, P.L. Grande and G. Schiwietz, Nucl. Instrum. and Meth. B 164-165 (2000) 203.
[41] P. Sigmund and A. Schinner, Phys. Rev. Lett. 86 (2001) 1486
[42] H. Weick, H. Geissel, C. Scheidenberger, F. Attallah, D. Cortina, M. Hausmann, G. Münzenberg, T. Radon, H. Schatz, K. Schmidt, J. Stadlmann, K. Sümmerer and M. Winkler, Phys. Rev. Lett. 85 (2000) 2725.
[43] Y. Vickridge et al., Europhys. Lett. 13 (1990) 635.
[44] F.Grüner, W. Assmann, F. Bell, M. Schubert, J. U. Andersen, S. Karamian, A. Bergmaier, G. Dollinger, L. Görgens, W. Günther and M. Toulemonde, Phys. Rev. B68 (2003) 174104.
[45] D. Dauvergne, A. Bräuning-Demian, F. Bosch, H. Bräuning, M. Chevallier, C. Cohen, A. Gumberidze, A. L'Hoir, R. Kirsch, C. Kozhuharov, D. Liesen, P-H. Mokler, J-C. Poizat, C. Ray, Th. Stohlker, M. Tarisien, E. Testa, S. Toleikis and M. Toulemonde, Nucl. Instrum. and Meth. B 205 (2003) 773.
[46] F. Grüner, M. Schubert, W. Assmann, F. Bell, S. Karamian and J.U. Andersen, Nucl. Instrum. and Meth. B 193 (2002) 165.
[47] V.V. Okorokov, Pisma Zh. Eksp. Teor. Fiz. 2 (1965) 175 (JETP Lett. 2(1965) 111.
[48] S. Datz, C. D. Moak, O. H. Crawford, H. F. Krause, P. F. Dittner, J. Gomez Del Campo, J. A. Biggerstaff, P. D. Miller, P. Hvelplund and H. Knudsen, Phys. Rev. Lett. 40 (1978) 843.
[49] S. Datz, C. D. Moak, O. H. Crawford, H. F. Krause, P. D. Miller, P. F. Dittner, J. Gomez Del Campo, J. A. Biggerstaff, H. Knudsen and P. Hvelplund, Nucl. Instrum. and Meth. 107 (1980) 15.
[50] M. Chevallier, C. Cohen, N. Cue, D. Dauvergne, J. Dural, P. Gangnan, R. Kirsch, A. L'Hoir, D. Lelièvre, J.F. Libin, P.H. Mokler, J.C. Poizat, H.T. Prinz, J.M. Ramillon, J. Remillieux, P. Roussel-Chomaz, J.P. Rozet, F. Sanuy, D. Schmaus, C. Stephan, M. Toulemonde, D. Vernhet, A. Warczak, Phys Rev. A. 61 (2000) 22742.
[51] N. Cue, J.-C. Poizat and J. Remillieux, Europhys. Lett. 8 (1989) 19.
[52] S.P. Møller, T. Worm, M. Clément, N. Doble, K. Elsener, L. Gatignon, P. Grafström, E. Uggerhøj, M. Hage-Ali and P. Siffert, Nucl. Instrum. and Meth. B84 (1994) 434.
[53] G. Arduini, C. Biino, M. Clément, K. Cornelis, N. Doble, K. Elsener, G. Ferioli, G. Fidecaro, L. Gatignon, P. Grafström, M.Gyr, W. Herr, J. Klem, U. Mikkelsen, E. Weisse, S.P.

Møller, E. Uggerhøj,, A. Taratin, A. Freund, P. Keppler and J. Major, Phys. Rev. Lett. 79 (1997) 4182.

Figure Captions

Figure 1. Formation of a shadow cone and of a blocking cone.
Figure 2. Normalized close nuclear encounter probability as a function of penetration depth for a 10 MeV proton beam entering an Au crystal, parallel to a <011> direction. This probability is obtained by Monte-Carlo simulations of sequences of binary collisions. The data are from ref. [17].
Figure 3. Normalized ion flux variation with penetration depth at distances larger than 1.2 Å from atomic strings for a 10 MeV proton beam entering an Si crystal, parallel to a <011> direction. This flux is obtained by Monte-Carlo simulations of sequences of binary collisions.
Figure 4. a)- Potential map per unit charge in the plane transverse to a <110> direction in Si. This potential is averaged along <110>. The values corresponding to the isocontours are (in eV) 1: 0.5, 2: 1.5, 3: 2.25, 4: 5, 5: 15, 6: 21, 7: 50. b)- Electron density map in the same transverse plane. This density is also averaged along <110>. The values corresponding to the isocontours are (in electron.$Å^{-3}$) 1: 0.032, 2: 0.1, 3: 0.24, 4: 0.5, 5: 1.0, 6: 3.0, 7: 10.0, 8: 30.0. From ref. [12].
Figure 5. Blocking pattern in the vicinity of a <110> direction of Si. This pattern corresponds to the angular distribution of 24 MeV/u U ions after elastic scattering on crystal atoms. The inset represents the axial blocking dip after averaging over the azimuth. From ref. [5].
Figure 6. Close nuclear encounter yield as a function of the tilting angle of a ^{3}He beam with respect to the <100> direction of a W crystal. o: backscattering yield on W atoms. Δ: proton yield from the D(^{3}He,p)^{4}He reaction on implanted deuterium. Two numerical simulations of this latter yield are also represented assuming that D atoms occupy either octahedral sites (dotted line) or tetrahedral sites (full line). The comparison with experimental results shows that the D atoms occupy the tetrahedral sites. The data are from ref. [21].
Figure 7. Angular scans across the [011] axis 45° off the (001) surface plane of a GaAs crystal, corresponding to the backscattering of 1 MeV ^{4}He ions. a): the comparison between the scans corresponding to the substrate and to an as-deposited Fe layer demonstrates that the latter is under compressive strain in the (001) plane. b): after heating at 450°C, an interfacial FeGaAs forms, and the remaining Fe surface film is now under tensile strain in the (001) plane. From ref. [22].

Figure 8. Random (•) and <100> aligned (o) backscattering spectra obtained with a 2 MeV ^{4}He beam sent on a W crystal. Note the surface peak at the high energy edge of the aligned spectrum. The data are from ref. [2].
Figure 9. Calculation by numerical simulations, for various ion-target combinations, of the surface peak area, expressed in number of atoms per row. This area is represented as a function of the ratio between the two-dimensional rms thermal vibration amplitude ρ and the radius R of the shadow cone at the level of the second atom of the atomic string considered. The data are from ref. [23].

Figure 10. (•) Integral of the surface peak as a function of temperature measured for the backscattering of a 100 keV proton beam incident along the [101] axis of a Pb crystal with (101) surface. The backscattered ions are detected along the [011] direction. The full lines correspond to numerical simulations assuming the absence of any surface disordering; Simulation I: surface atom thermal vibration amplitude equal to that of bulk atoms. Simulation II: adjustment of thermal vibration amplitude of surface atoms in order to fit the experimental results below 450 K. The data are from ref. [24].

Figure 11. Backscattering spectra for 1 MeV ^{4}He ions incident along the [110] axis of (a) a clean Ag (111) surface and of Au-covered surfaces (b), (c), (d). The Ag surface peak decreases due to shadowing by Au atoms. The data are from ref. [2].

Figure 12. Evidence for step edge relaxation, perpendicularly to the terraces, on (4,1,0) Cu. The surface peak blocking dips corresponding to backscattering, in the vicinity of the [011] axis in the terrace's plane, of 200 keV ^{4}He ions sent parallel to [100], are asymmetrical. Upper part: clean surface; evidence for step edge contraction. Lower part: oxygen covered surface; evidence for step edge expansion. (•): experimental results. Lines: Monte-Carlo simulations with various hypotheses on the relaxation. From ref. [25].

Figure 13. Random and aligned backscattering spectra from a 2 MeV ^{4}He helium beam on a (110) Ni crystal, for increasing fluence of 80 keV Sb^+ ion implantation, inducing crystal damage. From ref. [26].

Figure 14. Comparison of three angular scans across the [111] axis of a W crystal, with 1.4 MeV ^{4}He incident ions. (a): backscattering events from two depth windows respectively centered around 1200 and 5000 Å. (b): L shell X-rays yield. (c): Comparison of backscattering and M shell X-rays yields. The data are from ref. [27].

Figure 15. Simulation of blocking dips, across the [110] axis of a Si crystal, for Z = 41 fission fragments originating from 29 MeV/u Pb nuclei incident 5° off the axis. Various fission time distributions are used. Solid lines; simple exponential decays with various decrements. Dashed line: two-component time distribution (see text). From ref. [28].

Figure 16. Blocking dips, across the [110] axis of a Si crystal, for fission fragments originating from U like nuclei after collision of 24 MeV/u ^{238}U, with target nuclei. The full lines correspond to fits performed assuming a two-component time distribution (see text). The dotted lines correspond to the best fits obtained assuming exponential time distributions. In the fits the influence of post-scission neutron emission is taken into account. The various dips correspond to various total neutron multiplicities $M_{n,}$, and thus to various initial excitation energies. From ref. [5].

Figure 17. Energy loss distributions obtained with 29 MeV/u incident Pb^{56+} ions transmitted through 1.1 μm of Si. <110> axial and random crystal orientations. The energy loss is normalized to the random energy loss value, and corrected from a Q^2 dependence (see text). The integrals are not normalized.

Figure 18. Emerging charge state distributions of 27 MeV/u incident Xe^{35+} ions transmitted through 20.7 μm of Si. Open circles: random conditions ($F_R(Q_{out})$. Full circles: <110> alignment ($F_C(Q_{out})$. From ref. [12].

Figure 19. Tilt angle dependence of $F_C(Q_{out}=37)$ and Ly_α yield, in the vicinity of the <110> direction of a 20.7 μm Si crystal, for incident Xe^{35+} at 27 MeV/u. From ref. [12].

Figure 20. Average transverse energy (per unit charge), and mean sampled electron density, as a function of emerging charge Q_{out}, for incident Xe^{35+} at 27 MeV/u sent on a 30.7 thick silicon crystal along the <110> axis. From ref. [12].

Figure 21. Emerging charge state distributions for 29 MeV/u incident Pb^{56+} ions transmitted through 1.1 μm of Si in <110> axial and random conditions.

Figure 22. Energy loss distributions, backward and forward electron multiplicity distributions obtained with 29 MeV/u incident Pb^{56+} ions transmitted through 1.1 μm of Si. (a) <110> axially channeled ions emerging with Q_{out}=56. The inset in the first plot shows the selection of ions with the lowest energy loss. The electron multiplicity distributions corresponding to this selection are shown. (b) ions emerging with Q_{out} = 72, <110> and random conditions. The energy loss is normalized to the random energy loss value, and corrected from a Q^2 dependence (see text). The integrals of both multiplicity distributions and energy spectra are not normalized..

Figure23. Background subtracted charge state fraction $F_C(Q_{out}=32)/(F_C(Q_{out}=33)+F_C(Q_{out}=32))$ as a function of the incident energy of Br^{33+} ions channeled in a 1μm thick Si crystal, for 3 energy loss ranges, in units of the random energy loss: squares: 0.55-0.62, crosses: 0.48-0.55, triangles: 0.41-0.48. The data are from ref. [39].

Figure 24. X-ray spectra recorded at 90° in the laboratory for 60MeV/u Kr^{36+} ions incident on a 37μm thick silicon crystal. The spectra are normalized to the same number of incident ions. The solid lines show the calculated contributions of REC from valence and core electrons, and bremsstrahlung. From ref. [8].

Figure 25. Expected evolution of the energy loss for channeled U^{91+} ions in the <110> axis of silicon. The experimental data (circle: most probable energy loss in channeling, square: loss for random orientation) are taken from ref. [45]. The random energy loss curve corresponds to SRIM calculations [38]. The dashed curve corresponds to the loss experienced by the best channeled ions.

Figure 26. Flux distributions for Y ions transmitted through a 3.4 μm thick silicon crystal, for various energies (at emergence). Right part : circular averaged distributions around the <100> axis. The incident ion energy decreases from the upper part (showing a cooling effect) to the lower part (showing a heating effect) of the figure. The data are taken from ref. [46].

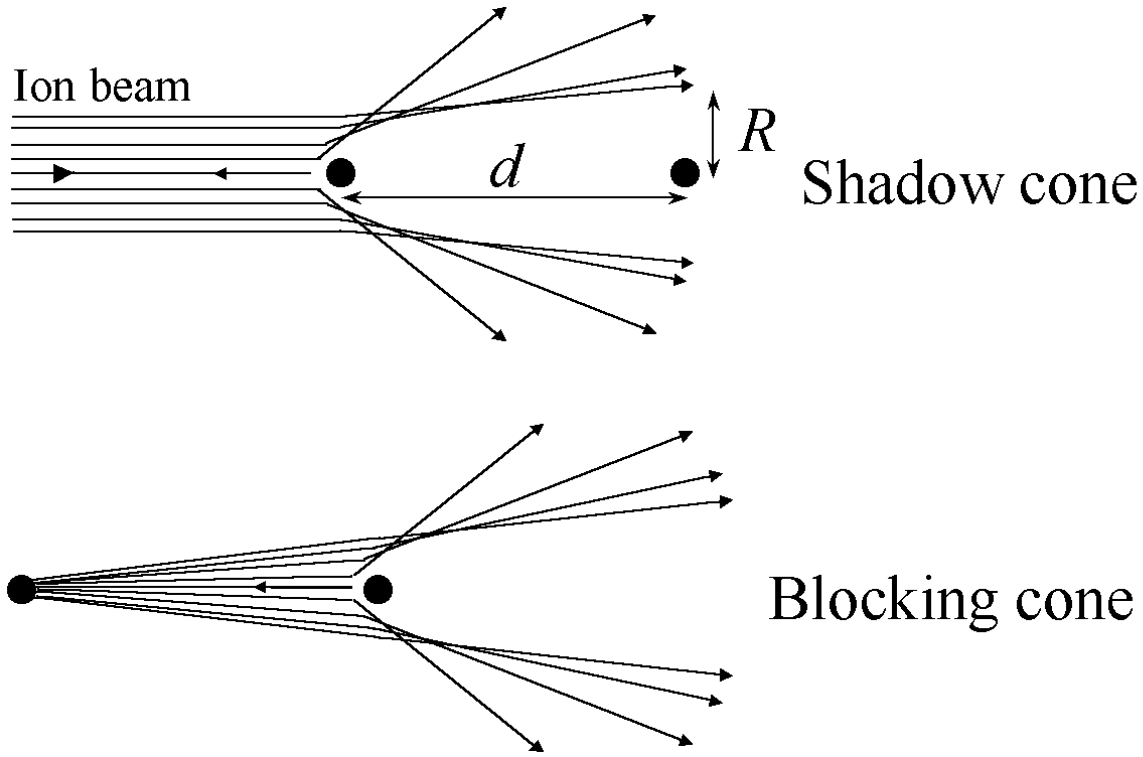

Figure 1

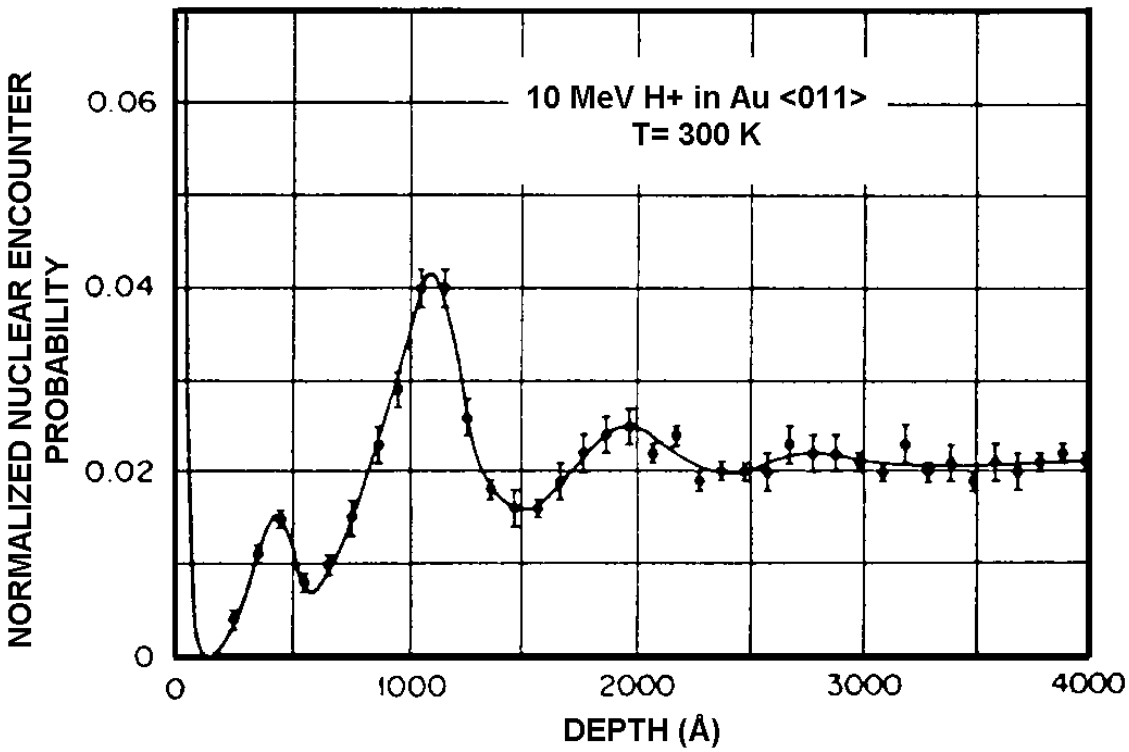

Figure 2

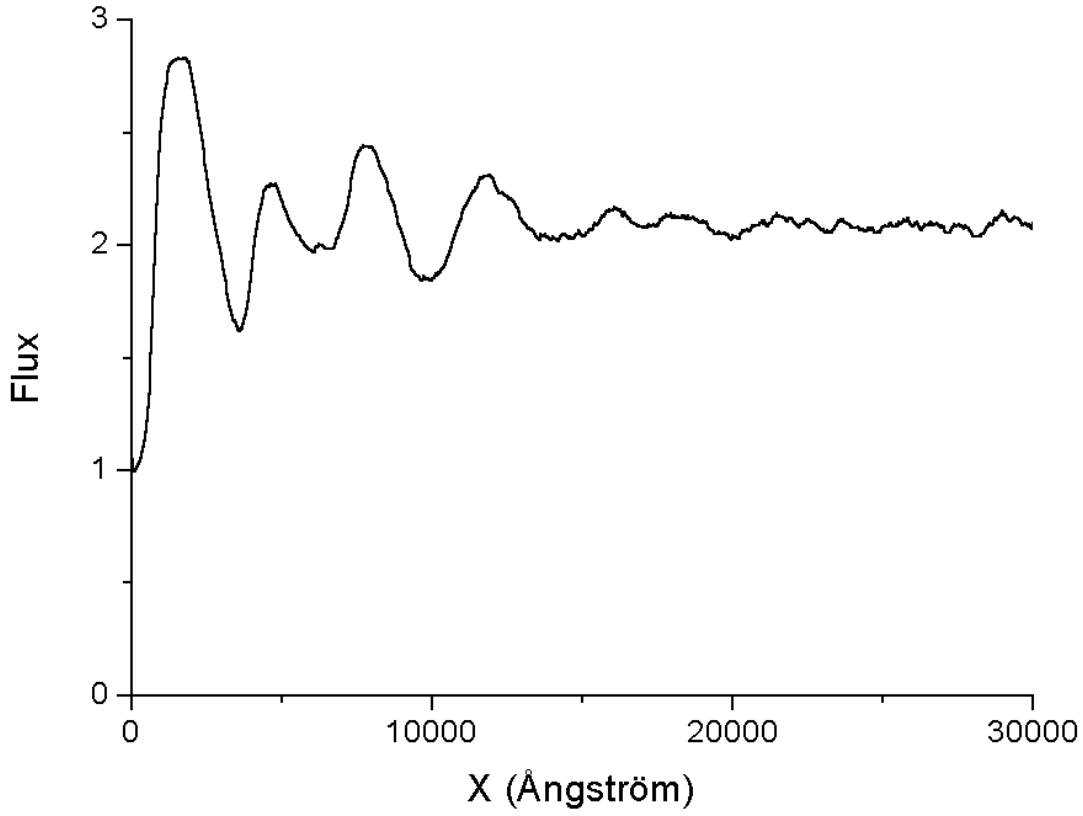

Figure 3

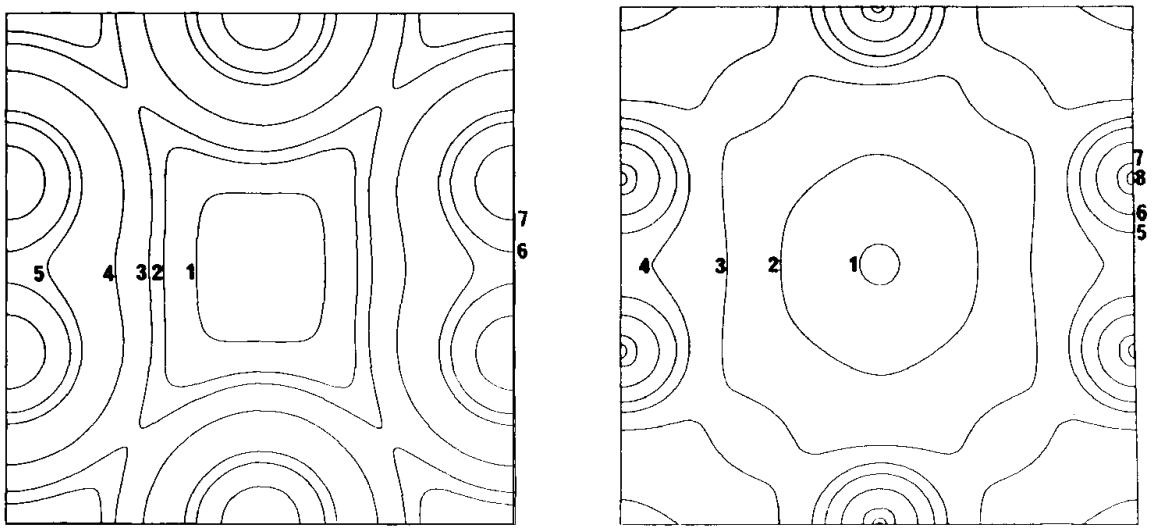

Figure 4

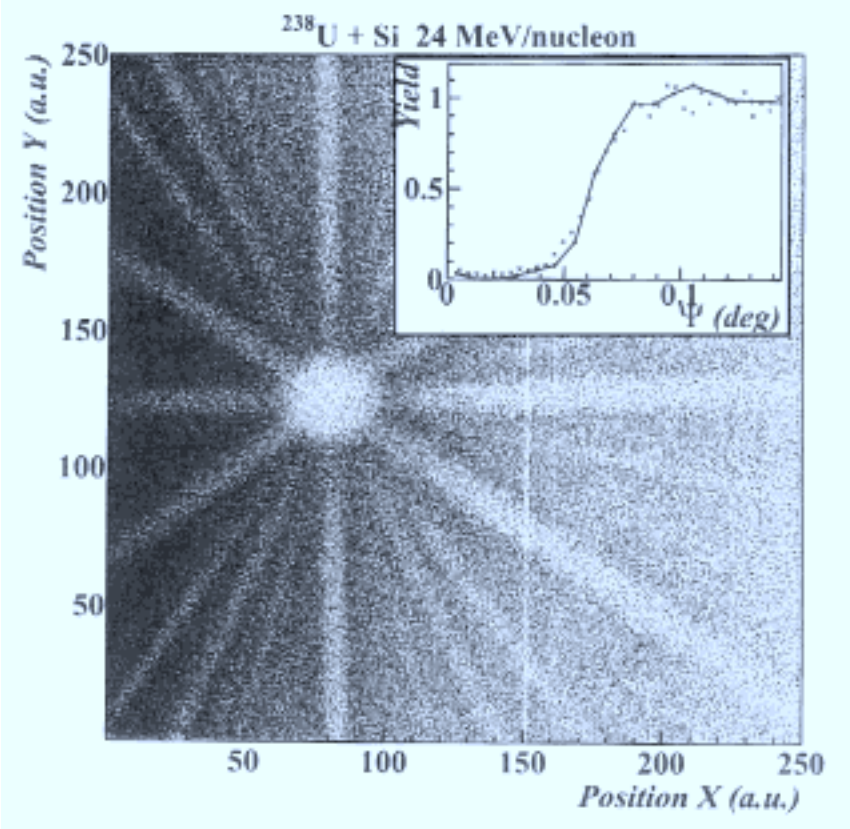

Figure 5

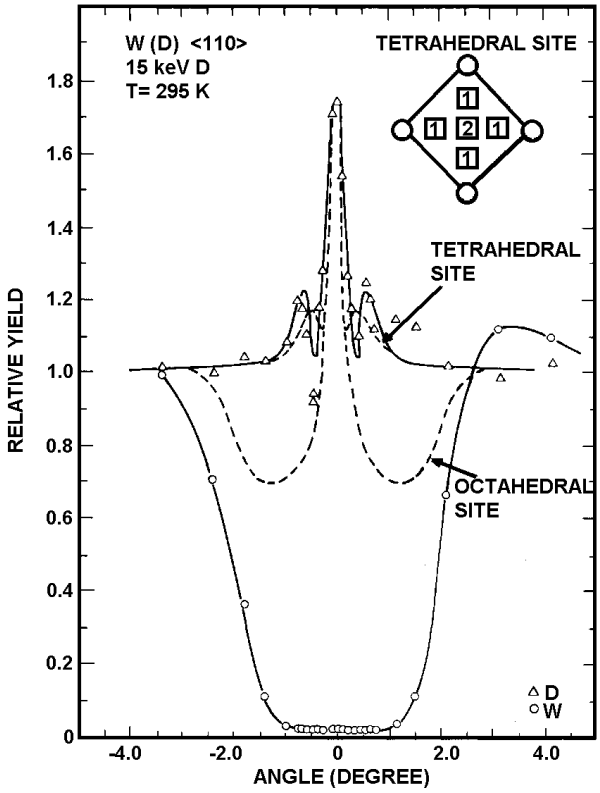

Figure 6

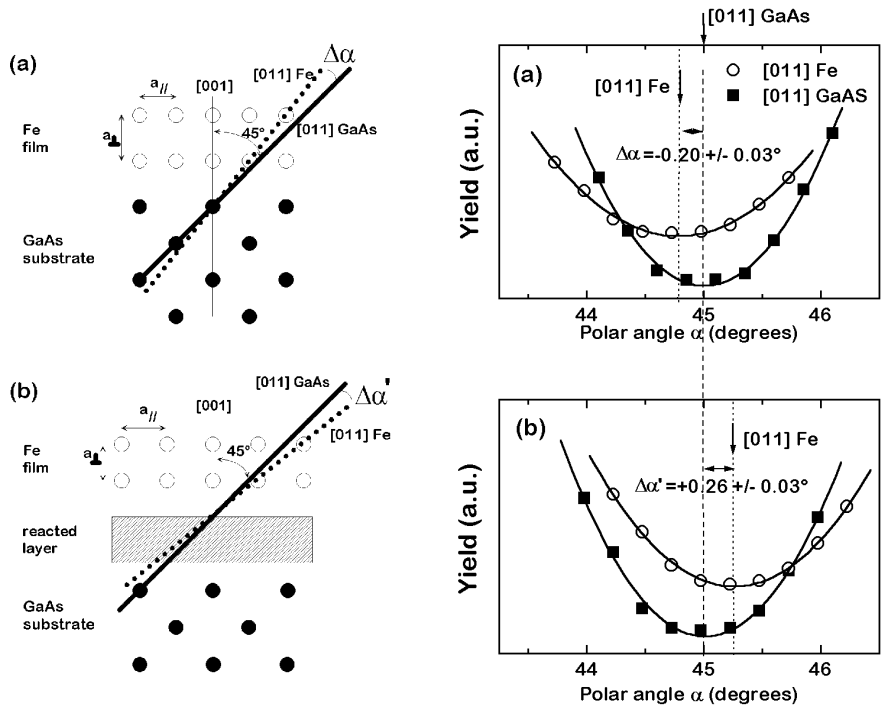

Figure 7

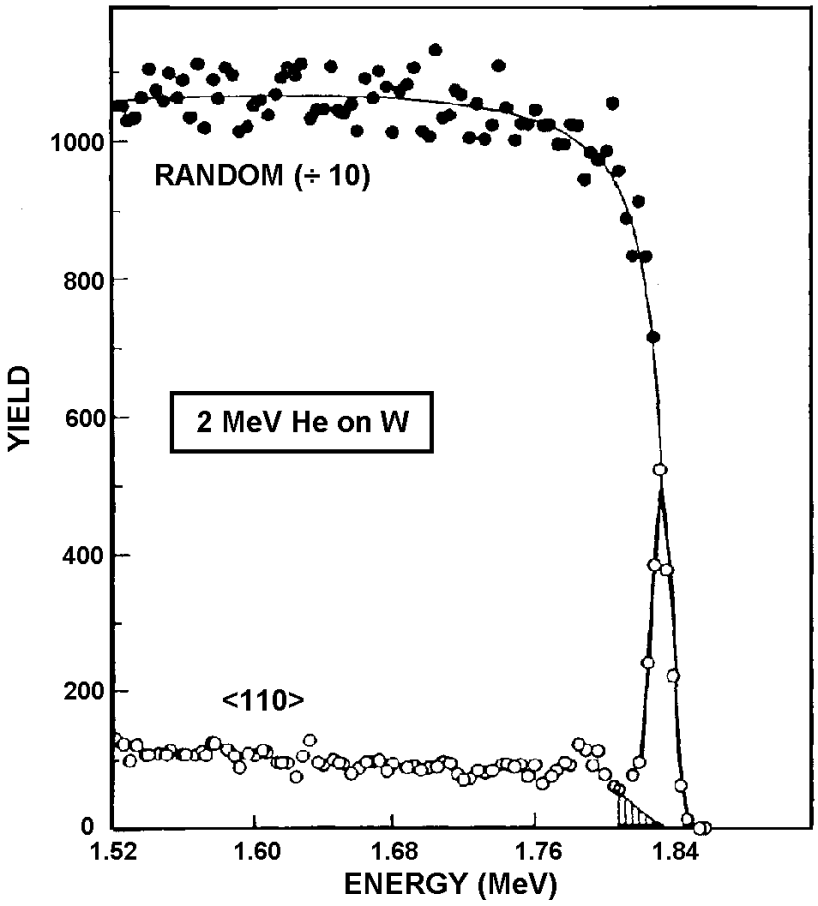

Figure 8

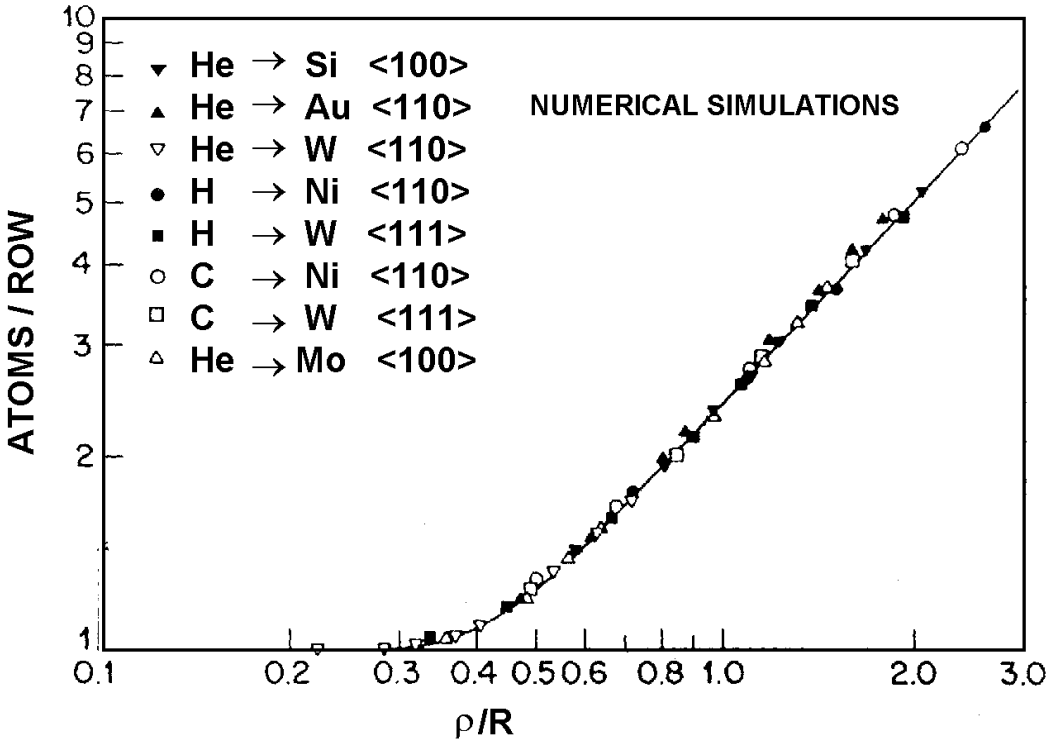

Figure 9

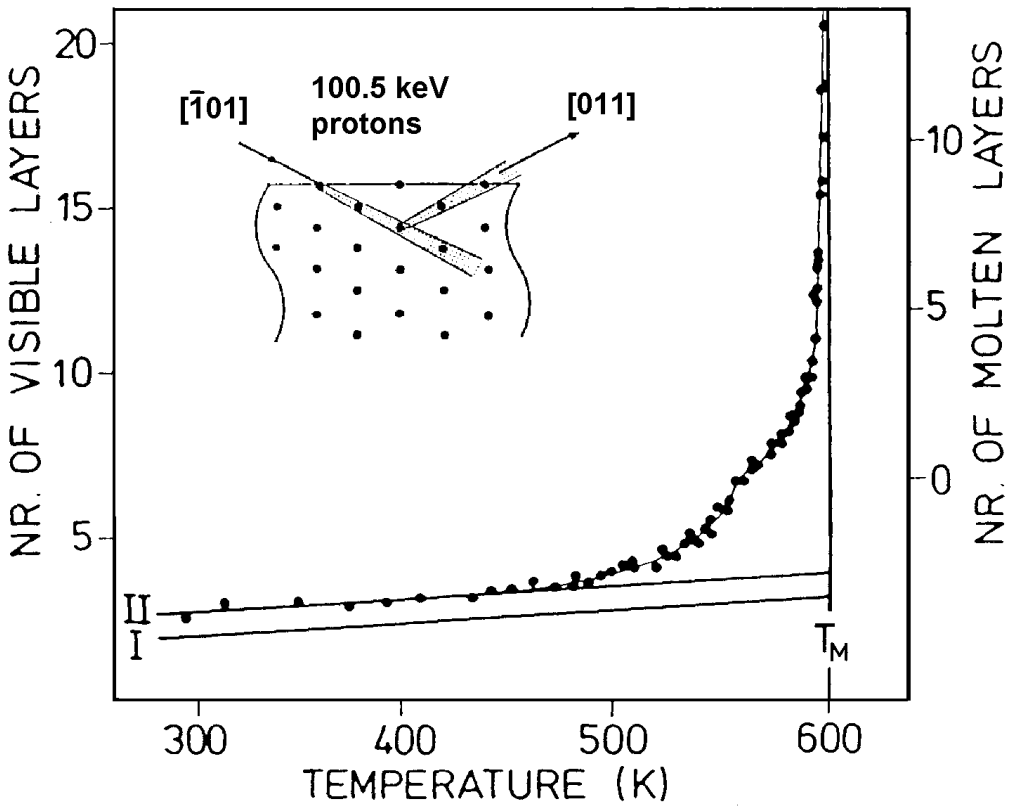

Figure 10

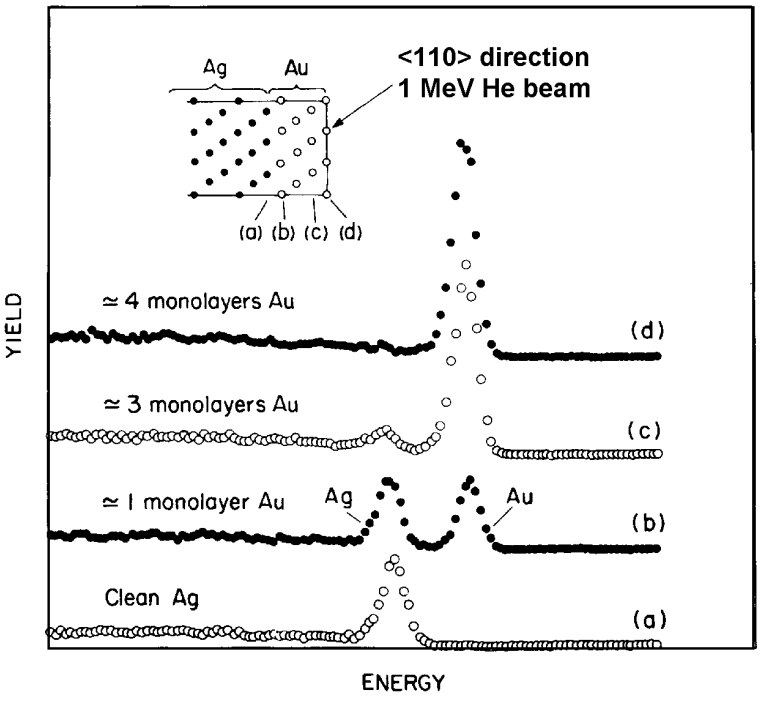

Figure 11

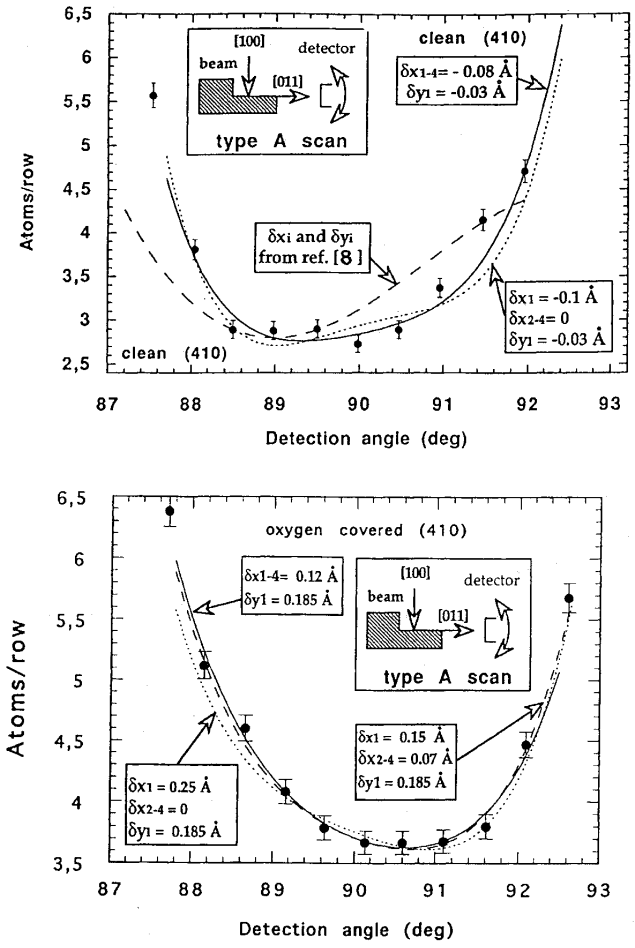

Figure 12

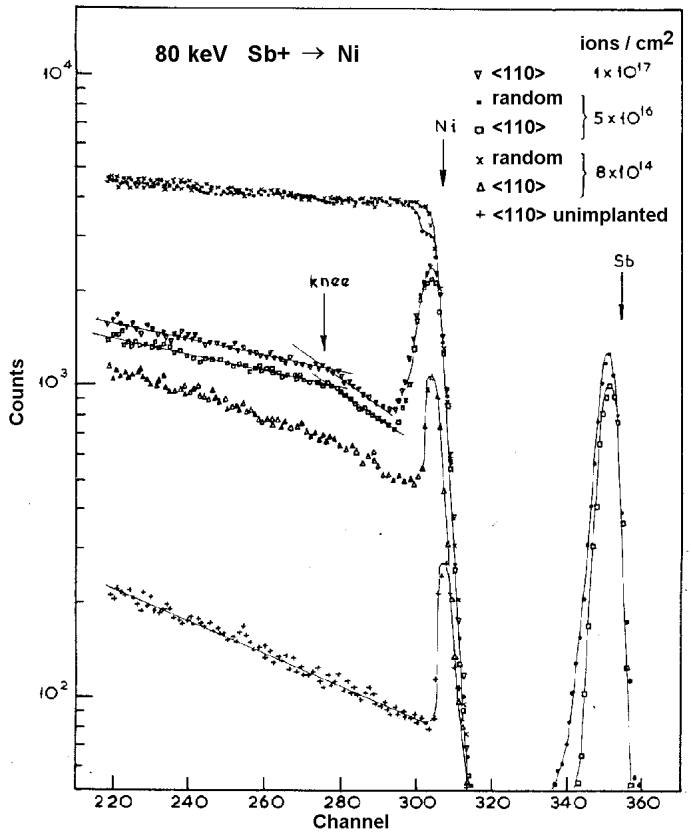

Figure 13

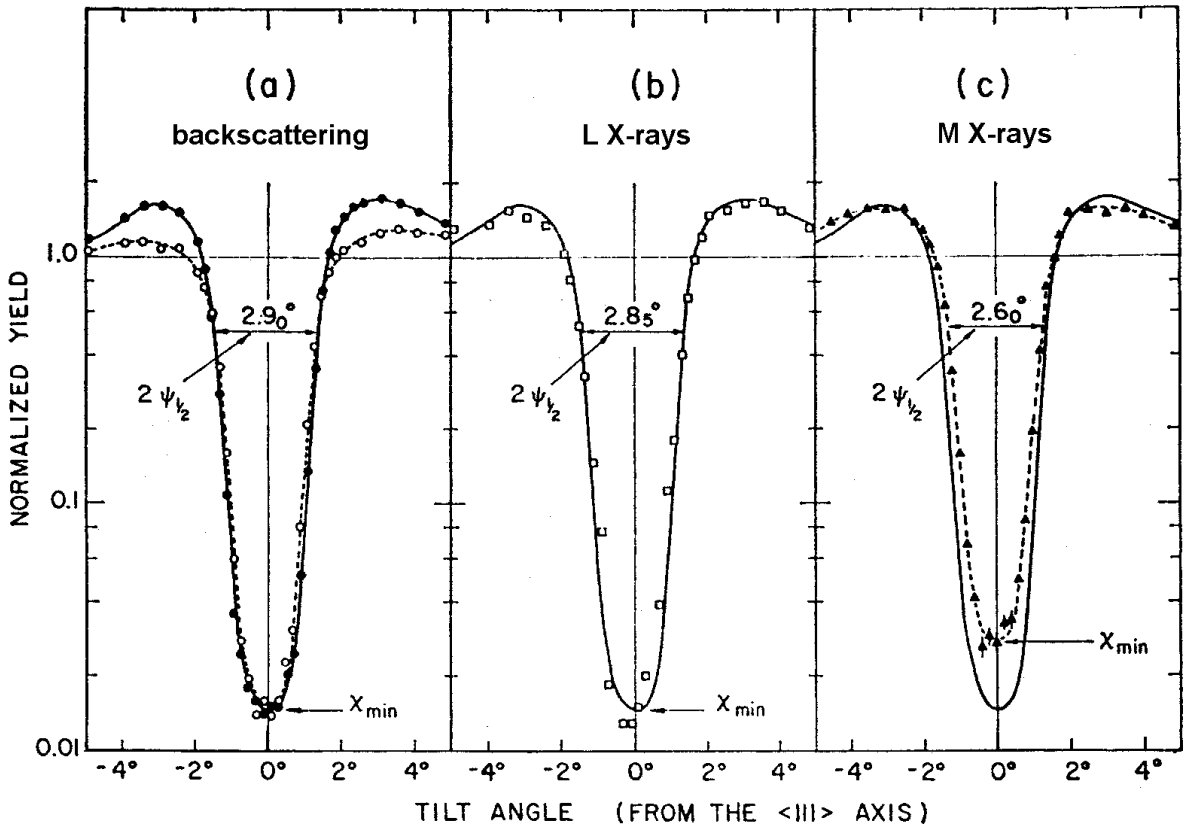

Figure 14

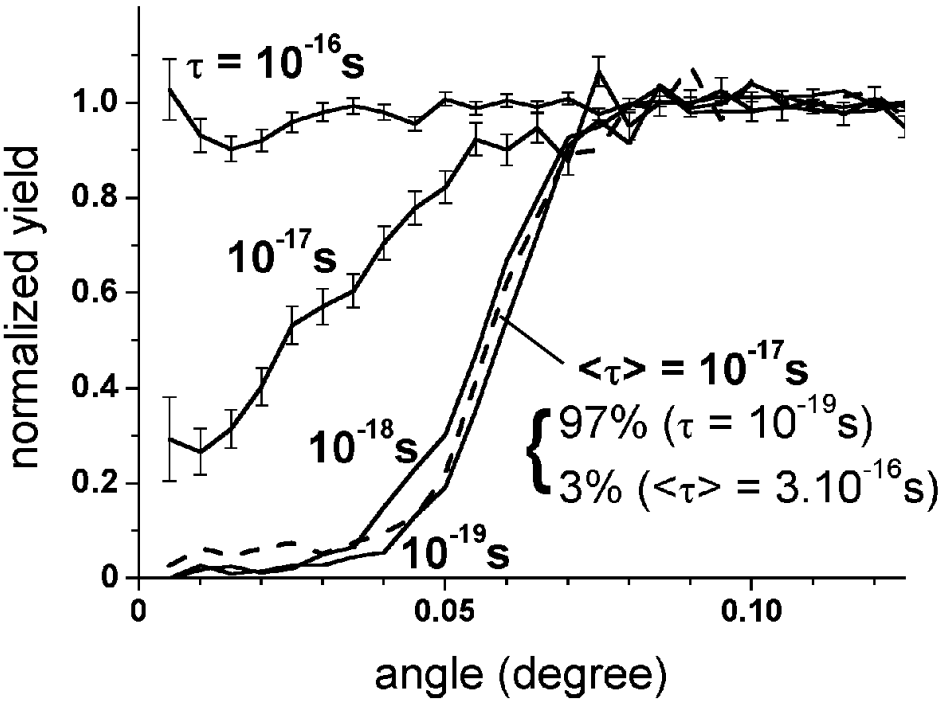

Figure 15

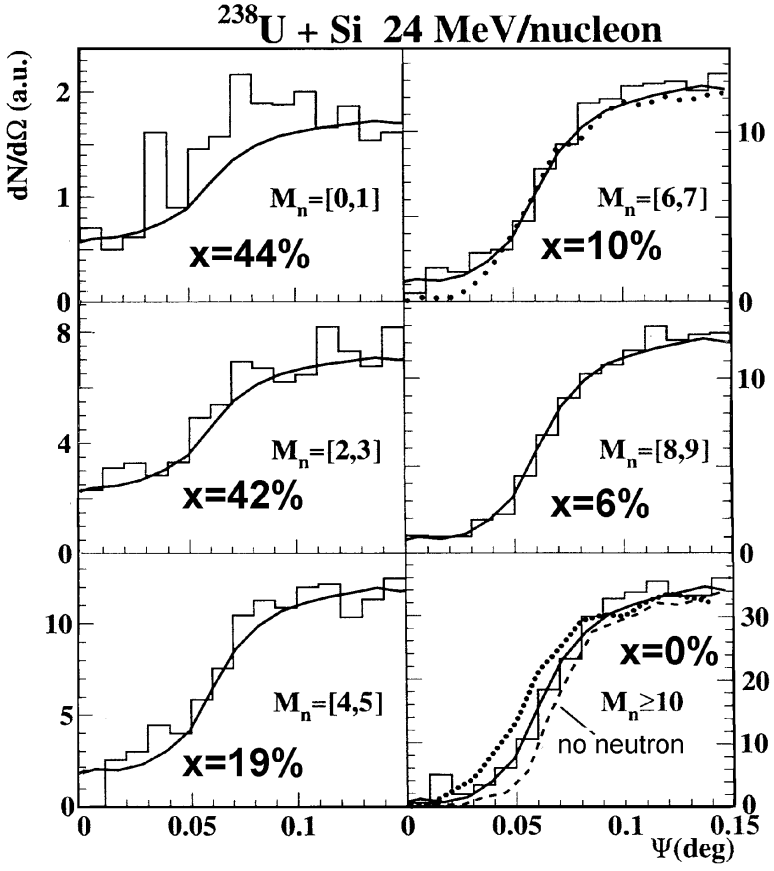

Figure 16

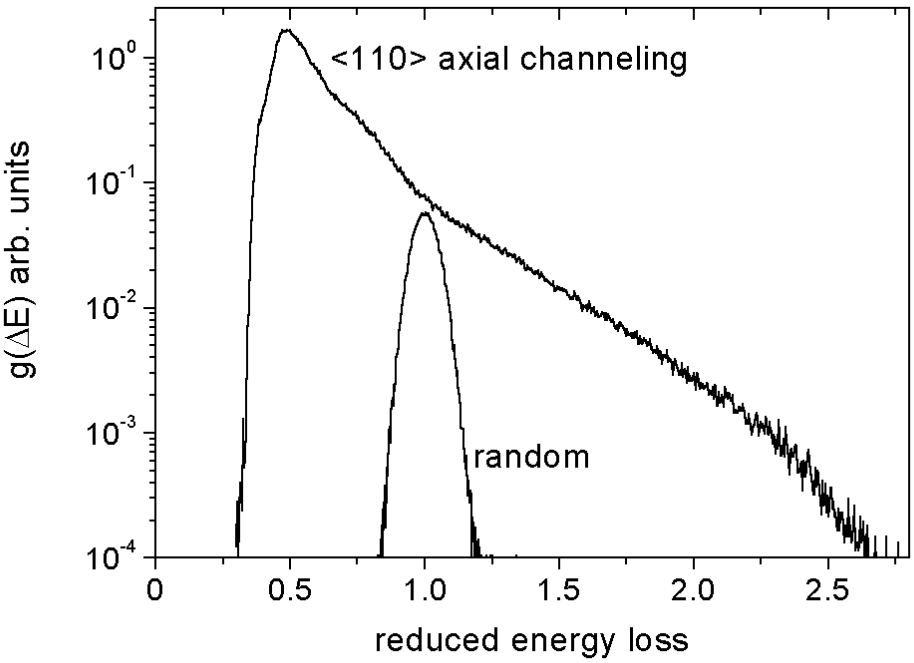

Figure 17

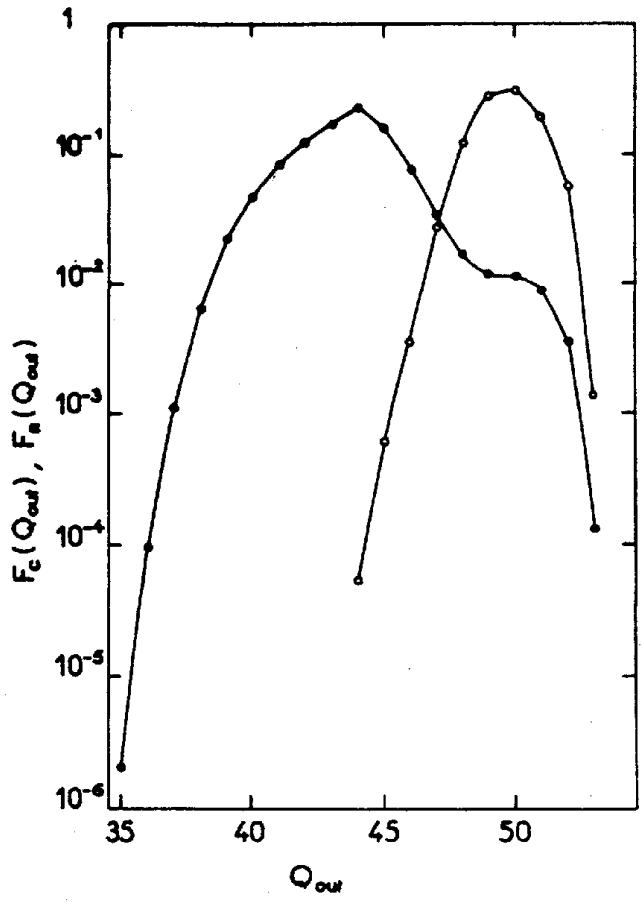

Figure 18

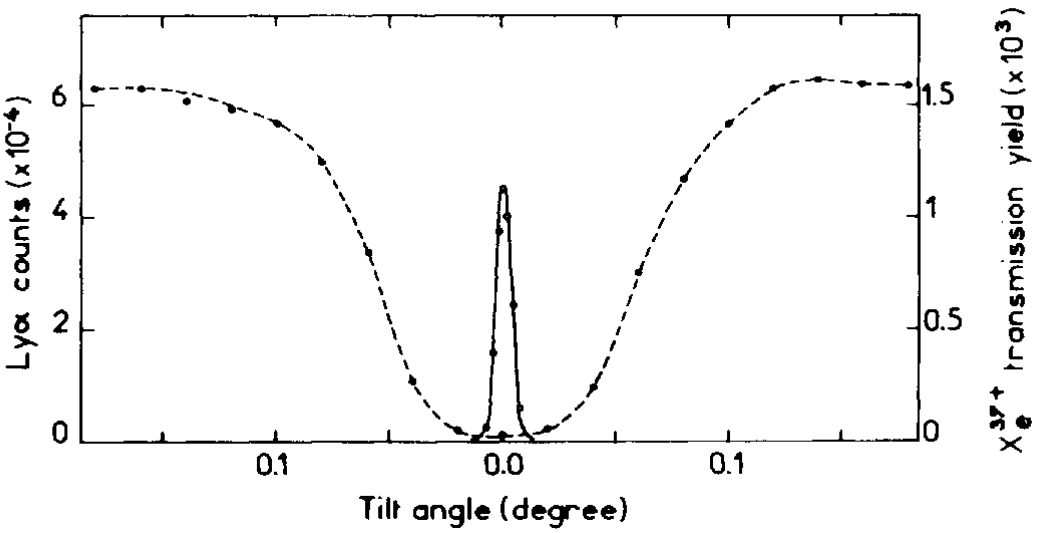

Figure 19

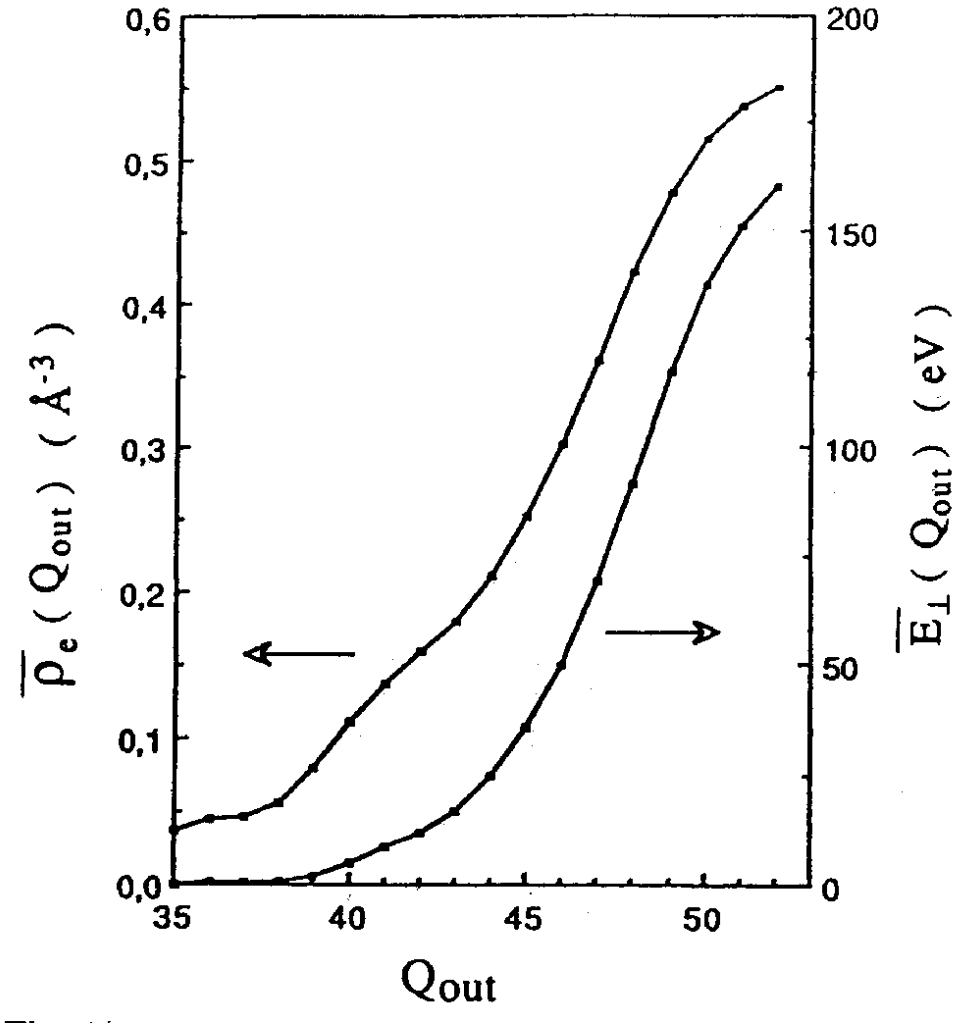

Figure 20

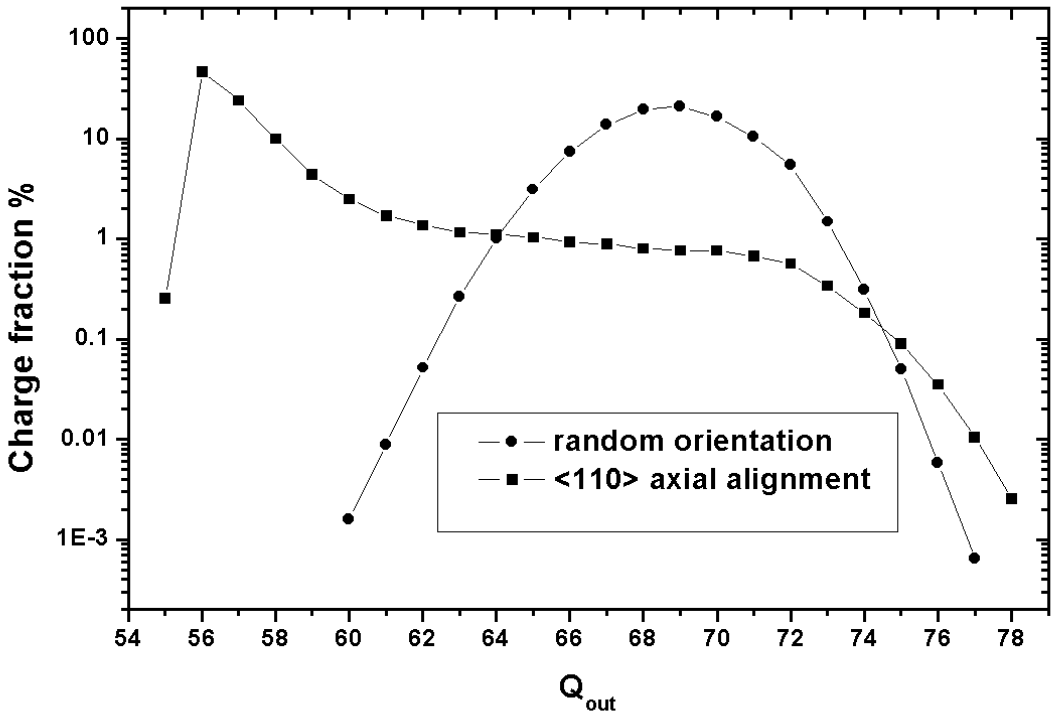

Figure 21

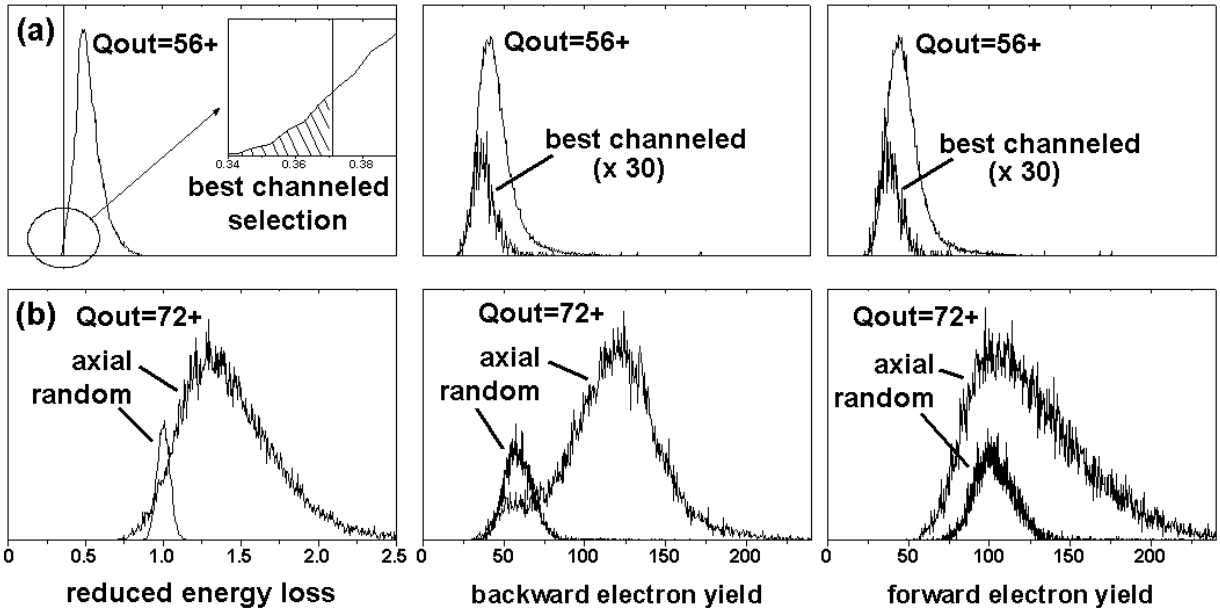

Figure 22

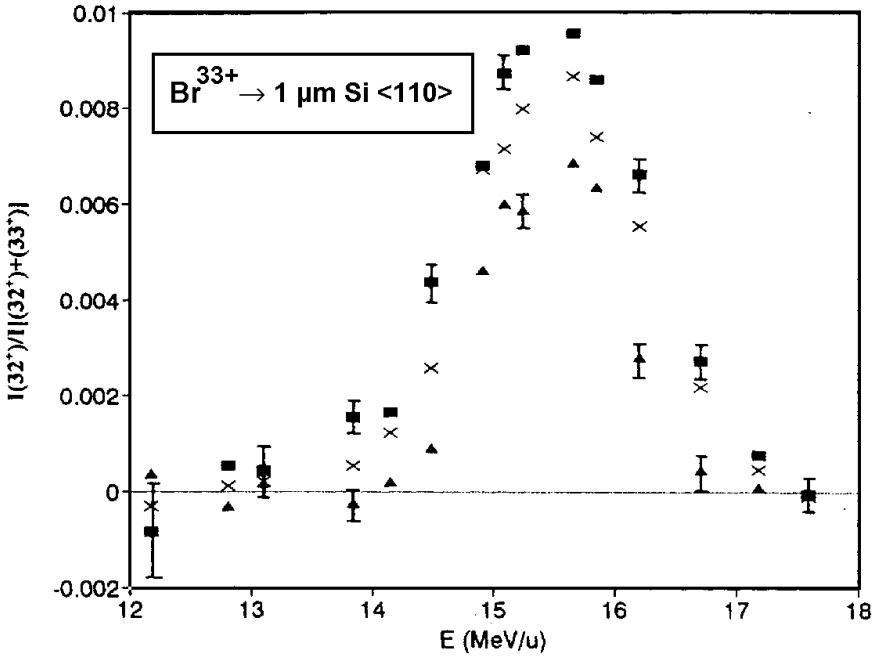

Figure 23

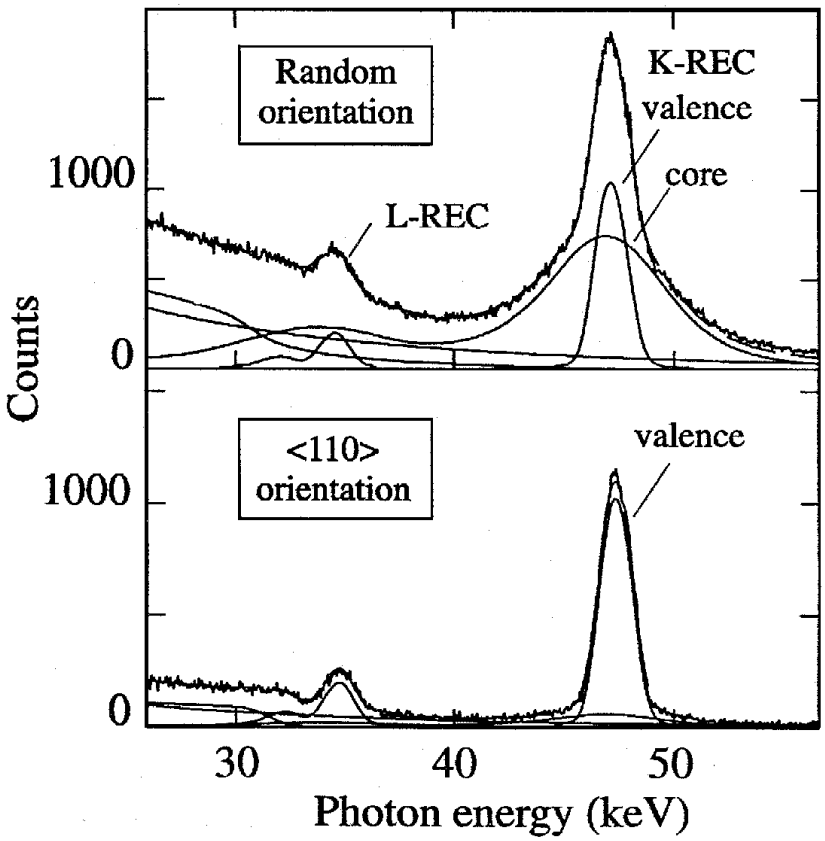

Figure 24

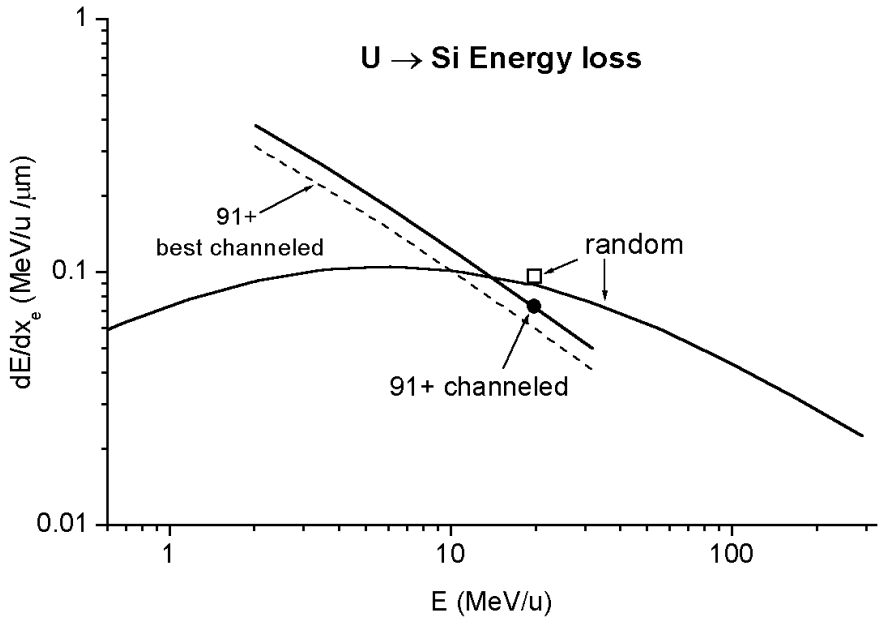

Figure 25

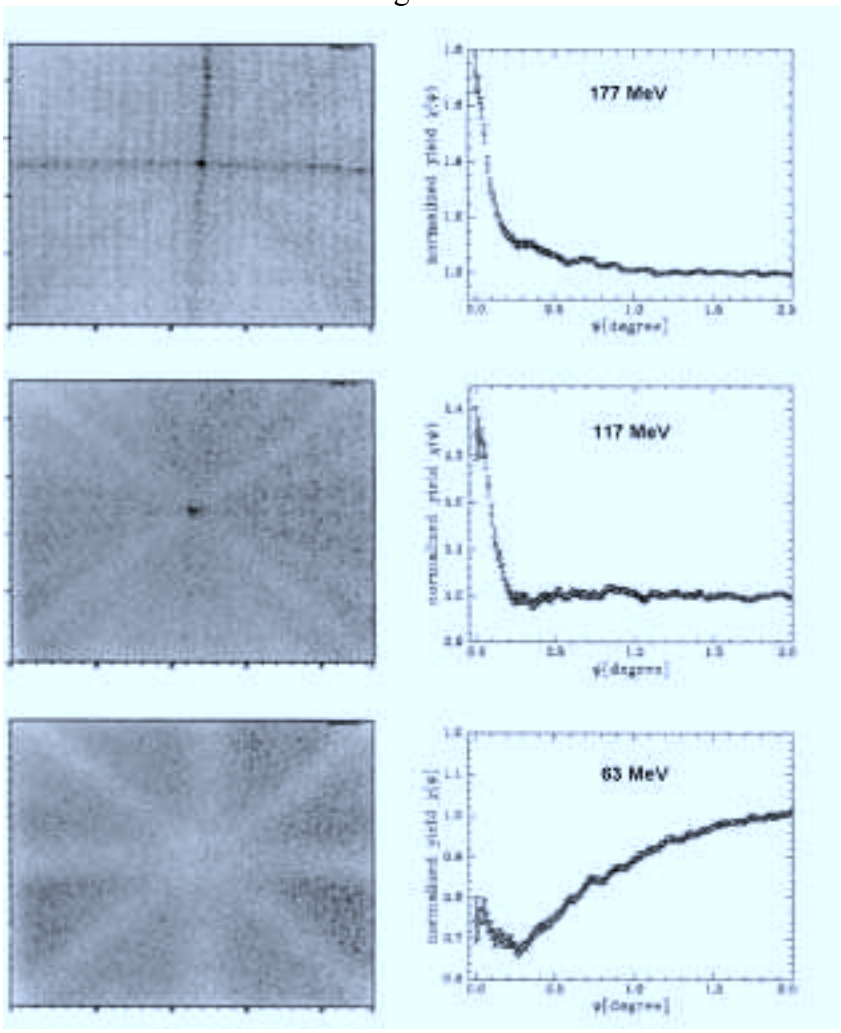

Figure 26